

# CRYOGENIC MULTILAYER INSULATION THEORY AND AN ANALYSIS OF SEAMS UNDER A VARIETY OF ASSUMPTIONS

*Thermal and Fluids Analysis Workshop 2018*

**J.P. Elchert**

*NASA Glenn Research Center*

*Thermal Systems Branch*

August 30, 2018

## 1 Abstract

The theory of thermal radiation as applied to cryogenic surfaces is explored and validation cases are solved in Thermal Desktop. Some results are compared to previously published research. Additionally, new results are published regarding cracks in both spherical and cylindrical cryogenic insulations with a cold boundary of 90 K to 220 K for ten layer blankets under a variety of assumptions and scenarios. It was found that enabling directional emission—as well as specular, mirrorlike reflections—have little impact on the results.

KEYWORDS: Cryogenic • Multilayer • Insulation • Superinsulation • Heat  
• Transfer • Thermal Control • Seams •

## Contents

<b>1</b>	<b>Abstract</b>	<b>1</b>
<b>2</b>	<b>Introduction</b>	<b>4</b>
<b>3</b>	<b>Theory</b>	<b>5</b>
3.1	Electromagnetic Radiation and Heat Transfer . . . . .	5
3.1.1	Blackbody Radiation . . . . .	5
3.1.2	The Plank Distribution . . . . .	6
3.1.3	Wien’s Displacement Law . . . . .	7
3.1.4	The Stefan-Boltzmann Law . . . . .	7
3.1.5	Band Emission . . . . .	7

3.2	Emission and absorption with real surfaces . . . . .	8
3.3	Directionally dependent optical properties . . . . .	9
3.4	Kirchhoff's Law . . . . .	10
3.5	The gray surface . . . . .	11
3.5.1	Concentric gray-diffuse spheres example . . . . .	12
3.6	Specularly Reflecting Surfaces . . . . .	14
3.7	Monte Carlo ray tracing . . . . .	16
3.7.1	Monte Carlo ray tracing . . . . .	16
3.7.2	Rays per node . . . . .	18
3.8	Non-gray . . . . .	21
3.8.1	Srinivasan's paradox . . . . .	21
3.8.2	Kauder's finite non-gray parallel plates example . . . . .	23
<b>4</b>	<b>Modeling superinsulation</b>	<b>23</b>
4.1	Floating shields analytical model . . . . .	23
4.2	Semi-empirical models . . . . .	24
4.2.1	Krishnaprakas's comparison . . . . .	29
4.2.2	Iterative separated mode model . . . . .	29
4.2.3	Seams and cracks in superinsulation . . . . .	29
4.2.4	Other models . . . . .	30
4.2.5	Other topics . . . . .	31
<b>5</b>	<b>Material Properties</b>	<b>31</b>
<b>6</b>	<b>Geometry</b>	<b>31</b>
<b>7</b>	<b>Boundary conditions</b>	<b>32</b>
<b>8</b>	<b>Validation Cases</b>	<b>32</b>
8.1	Optimizing rays per node and Bij/Fij cutoff factor . . . . .	32
8.2	Comparison to floating shields ideal solution . . . . .	32
8.3	Case 1: Floating shields, 3° crack, large isothermal surroundings, gray-diffuse . . . . .	33
8.4	Case 2: Floating shields, 3° crack, large isothermal surroundings, gray with directional emission . . . . .	33
8.5	Case 3: Floating shields, 3° crack, large isothermal surroundings, gray with directional emission and specular (mirrorlike) reflections . . . . .	33
8.6	Case 4: Floating shields, 6° crack, large isothermal surroundings, gray-diffuse . . . . .	33
8.7	Case 5: Floating shields, 12° crack, large isothermal surround- ings, gray-diffuse . . . . .	34
8.8	Case 6: Floating shields, 3° crack, surroundings brought very close, gray-diffuse . . . . .	34
8.9	Case 7: Contacting shields, 3° crack, large, isothermal surround- ings, gray-diffuse . . . . .	34

8.10 Case 8: Contacting shields, stronger contact, 3° crack, large, isothermal surroundings, gray-diffuse . . . . .	34
8.11 Non-gray case . . . . .	34
<b>9 Discussion</b>	<b>35</b>

## List of Symbols

$\dot{q}$	Heat Rate
$\rho$	Reflectivity
$\epsilon$	Emissivity
$\tau$	Transmissivity
$G$	Irradiation
$E$	Emission
$\lambda$	Spectral Wavelength
$T$	Temperature
$I$	Spectral intensity
$h$	Universal Plank constant
$c_o$	Speed of light
$k$	Boltzmann constant
$\sigma$	Stefan-Boltzmann constant
$C_{wien}$	Wien's constant
$\Gamma$	Band fraction of emission
$\alpha$	Band fraction starting wavelength
$\beta$	Band fraction ending wavelength
$R$	Radius of outer concentric sphere
$A$	Area
$\alpha$	Absorptivity
$\bar{\sigma}$	Root-mean-square roughness
$\omega$	Solid angle
$F$	View Factor
$A$	Area of cold boundary sphere
$r$	Radius of cold boundary sphere

## List of Subscripts

$\lambda$	Spectral Wavelength
$b$	Blackbody
$\alpha$	Band fraction starting wavelength
$\beta$	Band fraction ending wavelength

## 2 Introduction

Multilayer insulation (also called superinsulation or multi-layer or single-layer insulation or simply MLI) are thermal irradiation<sup>1</sup> or radiative emission barriers frequently used in systems where insulation is needed in a vacuum environment. To keep components either warm or cool, most spacecraft are covered with superinsulation (besides cut outs for radiators that reject heat to space). Some blankets—particularly ones applied to cryogenic systems—even provide some protection from micro-meteoroid orbital debris, atomic oxygen damage, electron charge accumulation, and rocket-engine plume impingement[11, p. 161].

A high reflectivity and zero transmissivity implies a low emissivity according to the energy balance, resulting in equation 1. More information on the derivation can be found in *Fundamentals of Heat and Mass Transfer* by Incropera and DeWitt [12, p. 757].

$$\rho_\lambda + \epsilon_\lambda + \tau_\lambda = 1 \quad (1)$$

A typical blanket is made up of a stack of layers of these low-emissivity films, such as a number of embossed, double-aluminized Kapton sheets, with or without a Dacron or silk spacer. The purpose of the embossed pattern or the spacers is simply to reduce conductive heat transfer through the random contacts between layers and spacers. A schematic of a cross section of a superinsulation blanket is shown in Figure 1.

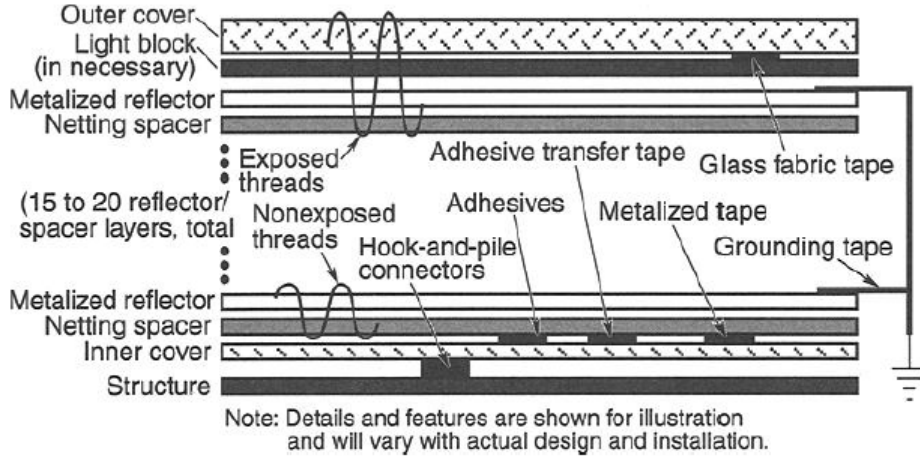


**Figure 1:** A schematic of a cross section of superinsulation, adapted from NASA [10].

Besides thermal insulation, blanket design is also constrained by requirements for durability, flammability, contamination control, launch loads, pressure decay, spacecraft venting, glint minimization, and magnetic materials, in

<sup>1</sup>From the perspective of an object, irradiation refers to incoming radiation.

addition to exposure to salt spray and other atmospheric exposure witnessed by materials on the launch pad[11]. Optimization also involves minimizing mass, cost, risk, and development time[11].

## 3 Theory

### 3.1 Electromagnetic Radiation and Heat Transfer

Typical forms of matter emit and absorb electromagnetic radiation and much of our modern understanding of this fact has its roots in the revolution in physics in the early twentieth century, after the notion of the luminiferous aether had been discarded. In particular, the discovery of the quantum and the blackbody spectrum helped spark a revolution in physics. The textbook *University Physics: Volume Two* by Ronald Lane Reese gives a comprehensive overview<sup>2</sup> and there are dozens of books on the history of modern physics.

In the next section, relevant concepts are briefly reviewed. Much of this material is adapted from *The Fundamentals of Heat and Mass Transfer*[12]. Note that this body of work only refers to heat transfer processes commonly found on various spacecraft<sup>3</sup>.

#### 3.1.1 Blackbody Radiation

Thermal radiation occurs between  $10^{-1} \mu\text{m}$  and  $10^2 \mu\text{m}$ . This encompasses part of the ultraviolet spectrum, the entire visible light spectrum, and the entire infrared spectrum. To understand thermal radiation, the concept of the blackbody and its properties should be defined as follows.

1. A blackbody absorbs all incident radiation, regardless of wavelength and direction
2. For a prescribed temperature and wavelength, no surface can emit more energy than a blackbody.
3. Although the radiation emitted by a blackbody is a function of wavelength and temperature, it is independent of direction. That is, the blackbody is a diffuse emitter.

No surface perfectly exhibits all of these ideal qualities. A cavity whose inner surface exhibits a uniform temperature is the closest approximation to a blackbody. Similarly, any small surface in the cavity experiences blackbody irradiation for which  $G_\lambda = E_{\lambda_b}(\lambda, T)$ . This surface is diffusely irradiated, regardless of orientation. Blackbody radiation exists within the cavity irrespective of whether the cavity surface is highly reflecting or absorbing.

---

<sup>2</sup>The *University Physics* volumes give a historical flavor to the subject that is helpful for beginning students and researchers.

<sup>3</sup>Rarified gases often behave in unexpected ways, like the solar corona, or interstellar dust, but these kinds of heat transfer processes are not discussed in this report.

### 3.1.2 The Plank Distribution

The blackbody spectral intensity is well known, having first been determined by Plank<sup>4</sup>.

$$I_{\lambda_b}(\lambda, T) = \frac{2hc_o^2}{\lambda^5(e^{\frac{hc_o}{\lambda kT}} - 1)} \quad (2)$$

Since the blackbody is by definition a diffuse emitter, it follows that the spectral emissive power, after integration, is simply the spectral intensity multiplied by  $\pi$ .

$$E_{\lambda_b}(\lambda, T) = \pi I_{\lambda_b}(\lambda, T) \quad (3)$$

An example of the Plank distribution plotted for a temperature of 20K is shown in Figure 2.

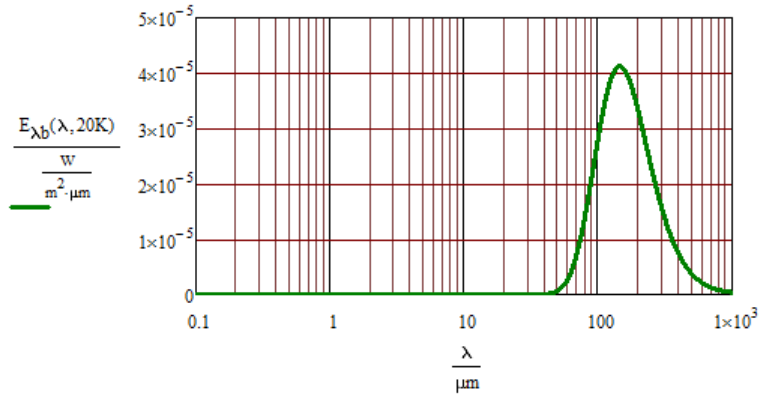


**Figure 2:** The famous Plank blackbody distribution, showing the emission spectrum for some blackbody at a temperature of 20K. This curve will shift to the left as the temperature of the blackbody increases.

In the Plank distribution, several things hold true:

1. The emitted radiation varies continuously with wavelength.
2. At any wavelength, the magnitude of the emitted radiation increases with increasing temperature.
3. The spectral region in which the radiation is concentrated depends on the temperature with comparatively more radiation appearing at shorter wavelengths as the temperature increases.

---

<sup>4</sup>The story of the resolution of the ultraviolet catastrophe of classical theory by Plank's discovery of the quanta—and its repercussions— is an amazing drama any student of history should examine.

4. A significant fraction of the radiation emitted by the sun, which may be approximated as a blackbody at 5800K, is in the visible region of the spectrum. In contrast, for T less than roughly 800K, emission is predominantly in the infrared region of the spectrum and is not visible to the eye.

### 3.1.3 Wien's Displacement Law

By differentiating with respect to wavelength and setting the result equal to zero, Wien's displacement law may be derived. The resulting equation is a simple relationship between the temperature of the blackbody and the wavelength at which peak radiation appears. Essentially, the blackbody spectral distribution has a maximum that depends on temperature.

$$\lambda_{max}(T) = \frac{C_{wien}}{T} \mid C_{wien} = 2898 \mu\text{m} \quad (4)$$

### 3.1.4 The Stefan-Boltzmann Law

By integrating equation 3 over the wavelength from zero to infinity, the Stefan-Boltzmann Law is obtained.

$$E_b(T) = \sigma T^4 \quad (5)$$

### 3.1.5 Band Emission

It is often necessary to know the fraction of total emission from a body over a certain band. This turns out to be a function of the product ( $\lambda T$ ), which is derived by integration. So there are tables that list the band fraction for given products. But with any computer algebra system, we can integrate directly.

$$\Gamma_{\alpha\beta}(\alpha, \beta, T) = \int_{\alpha}^{\beta} \frac{E_{\lambda_b}(\lambda, T)}{\sigma T^4} d\lambda \quad (6)$$

As an example, for 90K, considering a band up to 250  $\mu\text{m}$  would account for 99% of the energy emitted. For 220K, a band up to 102  $\mu\text{m}$  needs to be considered to account for 99% of the energy (these results are shown in Figure 3).

Relevant to cryogenic superinsulation heat transfer, consider that, in Figure 3, less than 1% of the energy is in the band from 250  $\mu\text{m}$  to 1000  $\mu\text{m}$  for the 90K case. The wavelength here is on the order of the spacing of the insulation (roughly 10 layers per centimeter means layer spacing is on the order of 0.1 cm which equals 1000  $\mu\text{m}$ ). At 20K, the energy in the 250  $\mu\text{m}$  to 1000  $\mu\text{m}$  band jumps drastically to 35%, with 1% of the energy having a wavelength between 1000  $\mu\text{m}$  and 10 000  $\mu\text{m}$ , which is greater than the spacing the layers. At 2K, 92% of the energy has a wavelength in this very long band from 1000  $\mu\text{m}$  and 10 000  $\mu\text{m}$  which is equivalent to 0.1 cm and 1 cm.

$$F_{\lambda_1\_to\_ \lambda_2}(\lambda_1, \lambda_2, T) := \int_{\lambda_1}^{\lambda_2} \frac{E_{\lambda b}(\lambda, T)}{\sigma \cdot T^4} d\lambda$$

$$\begin{aligned} F_{\lambda_1\_to\_ \lambda_2}(0\mu m, 250\mu m, 90K) &= 0.99058435978 \\ F_{\lambda_1\_to\_ \lambda_2}(0\mu m, 102\mu m, 220K) &= 0.99050727574 \\ F_{\lambda_1\_to\_ \lambda_2}(250\mu m, 1000\mu m, 20K) &= 0.352060993733 \\ F_{\lambda_1\_to\_ \lambda_2}(1000\mu m, 10000\mu m, 20K) &= 0.014433547225 \\ F_{\lambda_1\_to\_ \lambda_2}(0\mu m, 250\mu m, 2K) &= 0.000000001308 \\ F_{\lambda_1\_to\_ \lambda_2}(250\mu m, 1000\mu m, 2K) &= 0.066875394433 \\ F_{\lambda_1\_to\_ \lambda_2}(1000\mu m, 10000\mu m, 2K) &= 0.919737281264 \end{aligned}$$

**Figure 3:** A computer algebra system, like MathCAD, is very useful to avoid the table lookup typically associated with band fractions.

So as the temperature decreases, the problem of quantum tunneling begins to affect superinsulation performance. In this report, the studied temperature regime is 90K to 220K, so these effects don't come drastically into play.

### 3.2 Emission and absorption with real surfaces

Optical properties are a function of wavelength, directionality, and temperature. In the case of emission, it's the temperature of the object. In the case of absorption, the temperature is that of the irradiating object. So the real, total, hemispherical emissivity is just the ratio of real emission to ideal blackbody emission<sup>5</sup> at the temperature of the object's surface [12, p. 746].

$$\epsilon(T) = \frac{\int_0^\infty \epsilon_\lambda(\lambda, T) E_{\lambda_b}(\lambda, T) d\lambda}{E_b(T)} \quad (7)$$

Similary, the equation for absorptivity can be written:

$$\alpha(T) = \frac{\int_0^\infty \alpha_\lambda(\lambda, T) G_{\lambda_b}(\lambda, T) d\lambda}{G_b(T)} \quad (8)$$

---

<sup>5</sup>Of course, equation 7 has already been integrated over the two possible directions, zenith and azimuthal. For more information on the development of this equation, consult either *The Fundamentals of Heat and Mass Transfer* by Incropera and DeWitt or *Thermal Radiation Heat Transfer* by Siegel and Howell.



### 3.3 Directionally dependent optical properties

In his publication *Spacecraft Thermal Control Coatings References*, author Lonny Kauder supplies a derivation of directional emissivity curves for a typical dielectric and a typical conductor[14]. This derivation is not repeated here<sup>6</sup>, but some of the results are used in various Thermal Desktop (TD) models in this report. In short, Maxwell's equations, given a few assumptions, can be used to describe the interaction of electromagnetic radiation with spacecraft coatings, if the conductivity, permittivity, and permeability of the coating are known[14].

The graphs for typical, but hypothetical, emissivity curves are shown below, which is important for this study because directionality is one of the aspects being evaluated. In particular, the curve for the metallic surface is used in the Thermal Desktop simulation of the seams later in this report.

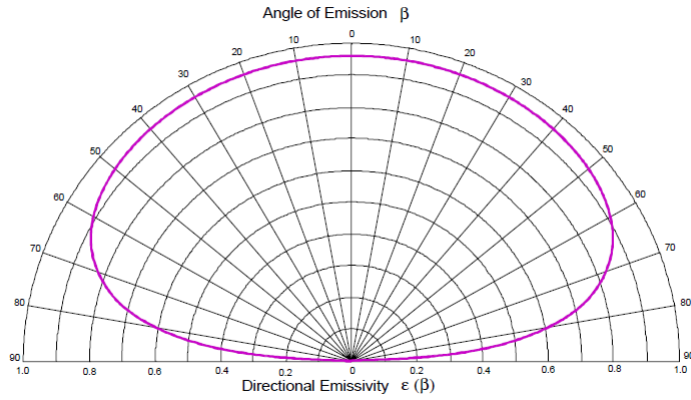


**Figure 4:** Directional emissivity curve for a dielectric with an index of refraction of  $n = 1.5$  [14]

On the ratio of hemispherical to normal, Siegel writes[23, p. 121],

For polished metals when  $\epsilon'_n$  is less than about 0.5, the hemispherical emissivity is larger than the normal value because of the increase in emissivity in the direction near tangency to the surface, as was pointed out in Figure 6. Hence, in a table listing emissivity values for polished metals, if  $\epsilon'_n$  is given, it should be multiplied by a factor larger than unity such as obtained from Figure 7[13].

So far, some attention has been paid on how to calculate the emissivity analytically. Interestingly, Kauder reveals that in practice, it is difficult to obtain the reflectance for any given coating over a wide enough wavelength range and at angles of incidence greater than twenty degrees for hemispherical emittance

<sup>6</sup>Kauder's derivations of the mathematics is clear and concise, and, in general, this is a very good resource for spacecraft thermal control coating properties.

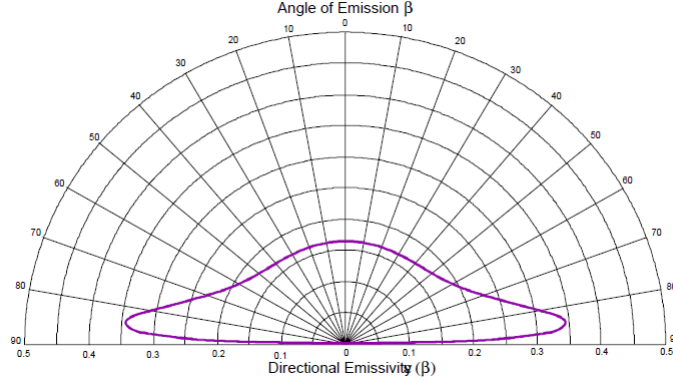


**Figure 5:** Directional emissivity curve for a conductor with an index of refraction of  $n=5.7+i9.7$  [14]

as a function of temperature calculations at cryogenic temperatures[14, p. 11]. Kauder writes,

[What can be done is] to obtain the reflectance at near normal angles of incidence from 1 to 200 microns. The emittance as a function of temperature can then be calculated assuming the coating to be Lambertian (perfectly diffuse). This assumption can lead to non-trivial errors in the calculated emittance since most coatings may not be diffuse, especially at longer wavelengths. The inherent error in the reflectance measurement at longer wavelengths is also a cause for increased error in the calculation. The result is an emittance temperature curve with nontrivial error bars.

### 3.4 Kirchhoff's Law

Consider a large, isothermal enclosure of temperature  $T_s$  within which several comparatively small bodies are confined. The irradiation from the walls is diffuse and equivalent to having come from a blackbody (blackbody cavity due to all the reflections and emissions), regardless of orientation. In steady state conditions,  $G = E_b(T_s)$  and all the bodies' temperatures equal to  $T_s$ . With simple math and conservation of energy, we can show that  $E_i(T_s)/\alpha_i = E_b(T_s)$  [12, p. 763] for every surface  $i$ . Since the absorptivity is less than or equal to one, this means that no real surface can emit more power than a blackbody at the same temperature. But it also shows that for any surface in the enclosure, total, hemispherical absorptivity equals the total, hemispherical emissivity.

Thus, for an isothermal enclosure, the absorptivity equals the emissivity for each surface. If the irradiation or the surface is diffuse, then the wavelength dependent (spectral) absorptivity equals the wavelength dependent emissivity. More generally, the directional and spectral absorptivity equals the directional

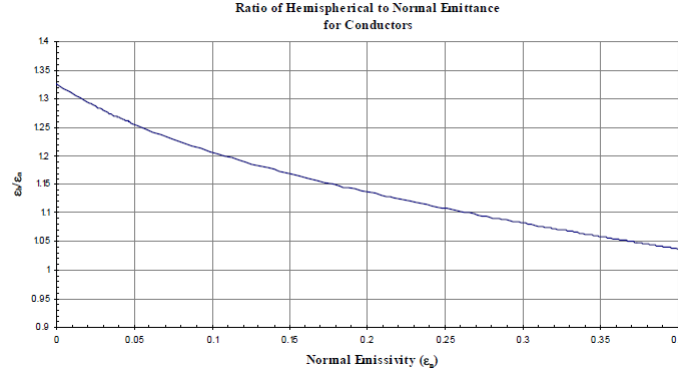


**Figure 6:** This relationship, derived from electromagnetic theory for a hypothetical ideal conductor, is where the often cited guideline that hemispherical emissivity is 1.3 times the normal emissivity originates [14].

and spectral emissivity. This thought experiment can be thought of as the basic conceptual definition of the gray surface[24].

### 3.5 The gray surface

The conditions under which the emissivity and absorptivity equations were derived, having to do with Kirchoff's Law, assumed irradiation due to emission from a blackbody at the same temperature as the surface. Clearly, this case is limiting. Luckily, the same mathematics can be extended to more cases if the diffuse-gray assumption may be applied. In other words, the absorptivity may be assumed to be equal to the emissivity.

For a surface to be considered gray, a pre-requisite is that either the irradiation is diffuse or the surface is diffuse (independent of direction). Diffuse irradiation is a reasonable approximation for many engineering calculations and the second condition is reasonable for many surfaces, particularly for electrically non-conducting materials. If either the irradiation corresponds to emission from a blackbody at the surface temperature, or if the surface is itself gray (independent of the spectrum) then the gray assumption holds. The gray assumption simply means the absorptivity is independent of wavelength over the spectrum of irradiation, and, similarly, the emissivity is independent of wavelength over the spectrum of emission.

Although the assumption of a gray surface is reasonable for many practical applications, some caution should be exercised in its use, particularly if the spectral regions of the irradiation and the emission are widely separated. It is possible for a coating to radiate heat to a surface for which there is little inherent ability to absorb the infrared energy while the integrated emittance and absorptance would give no hint of this problem [14, p.13].

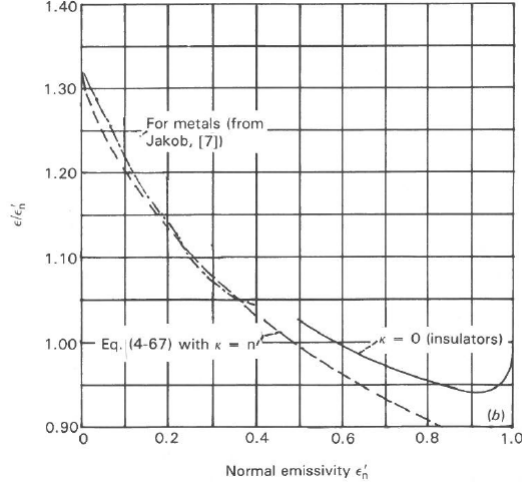


**Figure 7:** Ratio of hemispherical to normal emissivity for emission into air[13].

### 3.5.1 Concentric gray-diffuse spheres example

Typically, when solving basic radiation heat transfer network problems, we assume constant properties, gray-diffuse, steady state with no heat generation, and one dimensional heat transfer. In this case, the dimension of interest is the radius of the sphere. Gray refers to the idea that both the incident flux and emitted flux exist over the same wavelength such that the emissivity and absorptivity may be considered equivalent over the range of temperatures and photon wavelengths considered. We couple this assumption with diffuse because for the total emissivity and absorptivity to be equal, we also need to assume that there is no directionality associated with the radiation heat transfer process (in other words, reflections have no directionality associated with them).

Let the temperature of the outer sphere be 220K and the inner sphere be 90K (see Figure 8). Assume the inner radius is 0.5m and the inner sphere's emissivity is 0.3. The functional definition of radiation exchange between concentric spheres is given by equation 9. How does the heat transfer rate vary with radius and emissivity of the outer sphere?

$$\dot{q}(\epsilon_2, r_2) = \frac{\sigma A_1 (T_1^4 - T_2^4)}{\frac{1}{\epsilon_1} + \left( \frac{1-\epsilon_2}{\epsilon_2} \right) \left( \frac{R_1}{R_2} \right)^2} \quad (9)$$

Given these results, it seems we can expect that the more the outer sphere behaves like a blackbody, the worse the heat leak into the cryogenic tank. In other words, the smaller the outer sphere radius, and the more reflective it is, the lower the heat leak into the inner sphere. This shows one reason why closely spaced, metallic layers are better than layers spaced much further apart<sup>7</sup>.

<sup>7</sup>Of course, if the layers are too thin and closely spaced, then various other effects

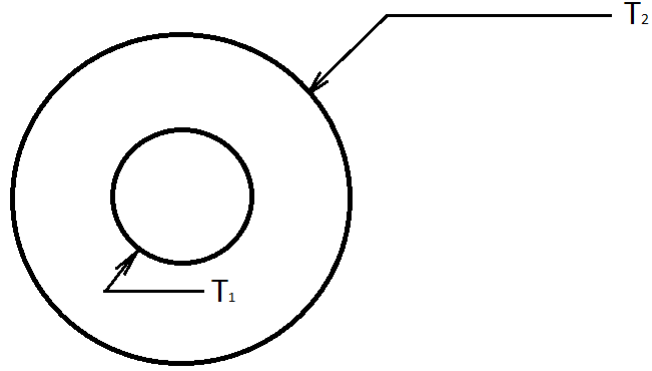


**Figure 8:** Radiation heat transfer between concentric cylinders

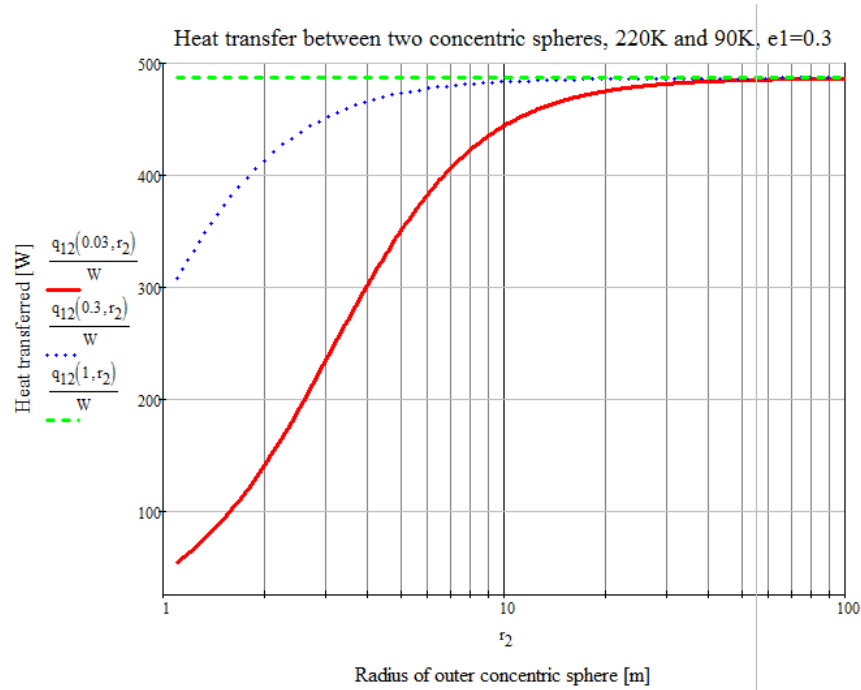


**Figure 9:** As the outer sphere tends towards a blackbody condition, the heat transfer is increased.

### 3.6 Specularly Reflecting Surfaces

Specular<sup>8</sup> reflection refers to mirror like reflection, distinct from emission as a function of the zenith or azimuth directions. As treated by Siegel and Howell in their comprehensive book, *Thermal Radiation Heat Transfer*, all of the surfaces in the example problem in this section are still assumed to emit in a diffuse manner<sup>9</sup> [23, p. 365]. Also, some of the surfaces are assumed to be specularly reflecting.

This kind of reflection arises, as written by the authors, because "for long wavelength radiation, a smooth surface tends toward being optically smooth, and the reflections tend to become more specular [23, p. 365]." In this way, a surface that isn't visibly smooth may yet be specular for longer wavelengths, and whether or not it is depends on the ratio of the root-mean-square roughness to the wavelength of radiation being considered<sup>10</sup>. If this ratio is much less than one, then the surface may be considered optically smooth for this problem and reflections treated specularly rather than diffusely.

$$\frac{\bar{\sigma}}{\lambda} \ll 1 \rightarrow \text{specular} \quad (10)$$

To better understand specular reflections and their relation to the geometry, comparing two idealized cases seems useful. For example, consider two infinite, gray, diffuse<sup>11</sup> parallel, specularly reflecting surfaces. Because all reflected radiation is heads directly back to the other surface, in this case, it turns out to not matter. The heat transfer equation is the same as the case with diffuse reflections[23, p. 367].

$$\dot{q}_1 = -\dot{q}_2 = \frac{A_1 \sigma (T_1^4 - T_2^4)}{1/\epsilon_1(T_1) + 1/\epsilon_2(T_2) - 1} \quad (11)$$

However, now consider radiation between concentric spheres, as shown in Figure 10. The view factors for an enclosure formed by two spheres are well known [12, p. 814].

$$F_{m,n} = \begin{pmatrix} F_{1,1} = 0 & F_{1,2} = 1 \\ F_{2,1} = A_1/A_2 & F_{2,2} = 1 - A_1/A_2 \end{pmatrix} \quad (12)$$

become important, like wave interference, tunneling, or just long wave reflections off the substrate[20][23, p. 375]. These effects are not considered in this work.

<sup>8</sup>Not to be confused with spectral dependence, which refers to wavelength dependence of optical properties.

<sup>9</sup>With Thermal Desktop software, the option to include both directional emissivity (relaxing the diffuse assumption) and specular reflections (at whatever fraction of reflected energy specified by the user) at will and both are studied systematically for the spherical geometry in this study, as described later in this report.

<sup>10</sup>Usually the peak can be considered but for the sake of completeness, this should be evaluated over the spectrum of emission.

<sup>11</sup>The surfaces can be considered directionally emitting; Siegel and Howell cover an example [23, p. 370] like this with two infinite plates where the solid angle  $d\omega$  describes the infinitesimal emitted radiation per unit area, which is integrated with the exchange factor in the integrand cite[p. 728]incro07

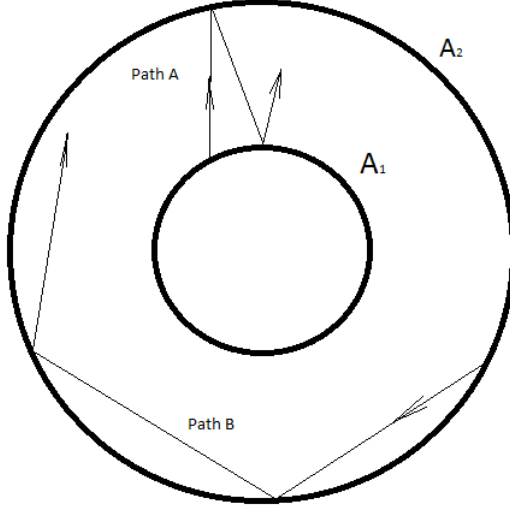


**Figure 10:** Some paths, like path B, won't reflect back to the opposing surface.

Clearly,  $A_1$  can only exchange radiation as if the two concentric surfaces were infinite parallel plates—regardless of specularity. In other words, none of the energy from  $A_1$  can ever be reflected off  $A_2$  twice in succession without first returning to  $A_1$  [23, p. 368]. But the emitted energy of fraction  $F_{2,2}$ , on the other hand, will consist of rays following paths like path B (Figure 10). What is so interesting about this is that because of the specularity of the reflections, none of this emitted energy will ever reach  $A_1$ . This removes the dependence of the size of  $A_2$  from the problem, and is what makes the specular result slightly different. This can be seen mathematically in equation 13.

$$\dot{q}_{1,1}(A_1, \epsilon_2, T_2) = A_2 \epsilon_2 F_{2,1} \sigma T_2^4 = A_2 \epsilon_2 (A_1/A_2) \sigma T_2^4 = A_1 \epsilon_2 \sigma T_2^4 \quad (13)$$

An example to illustrate the effect is useful because it has implications for superinsulation. Consider two concentric spheres as shown in 11. Assume the outer sphere is 220K and the inner sphere is 90K. The inner sphere emissivity is fixed at 0.02. How does the specular result compare to the diffuse result? The equation for specular heat transfer with this geometry is given by equation 14 whereas diffuse is equation 15. Notice that the dependence on the inner sphere area cancels out in equation 14 whereas there is no dependence on the outer sphere area (and thus no dependence on the annulus spacing) in equation 15.

$$\dot{q}_{12s}(r, t, T_1, T_2, \epsilon_1, \epsilon_2) = \frac{A_1(r) \sigma (T_2^4 - T_1^4)}{\frac{1}{\epsilon_1} + \frac{A_1(r)}{A_2(r,t)} \left( \frac{1}{\epsilon_2} - 1 \right)} \quad (14)$$

Note that if emissivity of the outer sphere equals unity in equation 14 or 15, then the equation reduces to the widely known form for large, isothermal

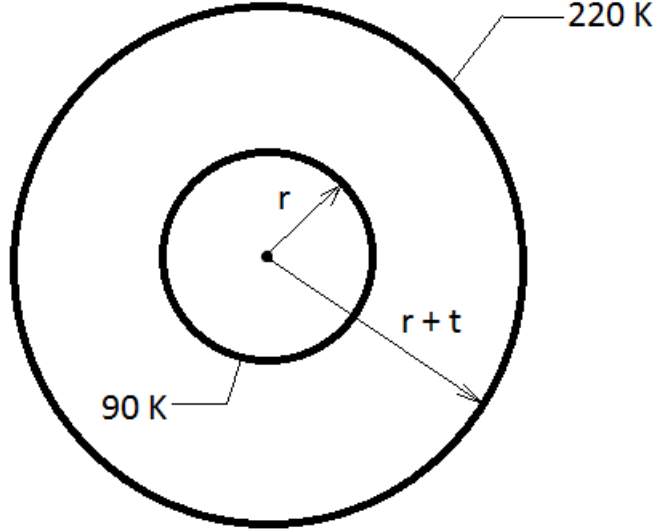


**Figure 11:** Concentric specular sphere heat transfer example showing the boundary conditions. The effect of different emissivities is evaluated, as well as the effect of a changing annulus size.

surroundings.

$$\dot{q}_{12}(r, t, T_1, T_2, \epsilon_1, \epsilon_2) = A_1(r) \sigma \epsilon_1 (T_2^4 - T_1^4) \quad (15)$$

Then the ratio of these two (equation 16) can be plotted as shown in Figure 12. These results show that the specular effect only dominates at large radii. As previously discussed, when closely spaced, the system begins to behave more like infinite planes, and it was already shown that both the specular and diffuse forms of this case are identical. So another reason why thin, closely spaced layers work for superinsulation is because it minimizes the specular effect. Of course, what happens to the specular effect in the presence of seams is considered later in this report.

$$\dot{q}_{ratio}(r, t, T_1, T_2, \epsilon_1, \epsilon_2) = \frac{\dot{q}_{12}(r, t, T_1, T_2, \epsilon_1, \epsilon_2)}{\dot{q}_{12s}(r, t, T_1, T_2, \epsilon_1, \epsilon_2)} \quad (16)$$

### 3.7 Monte Carlo ray tracing

#### 3.7.1 Monte Carlo ray tracing

Using Thermal Desktop and the RadCAD module, radiation conductors (radks), view factors, or heating rates can be output for input into SINDA/FLUINT<sup>12</sup>,

<sup>12</sup>The original version, CINDA, was developed in the 1960s in a partnership between Chrysler and NASA.



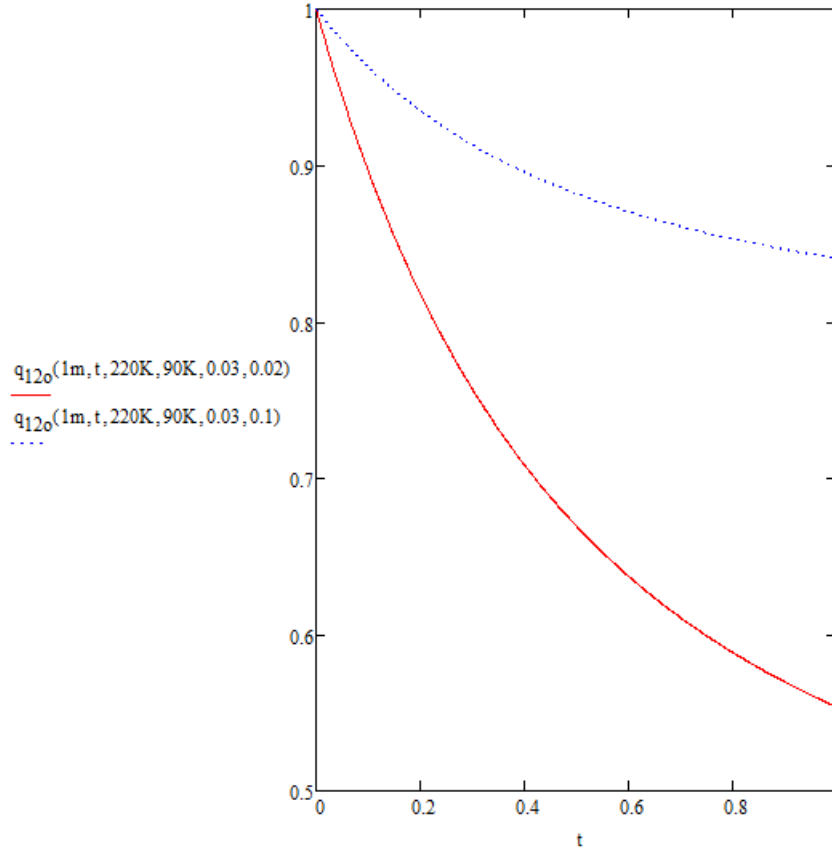


**Figure 12:** These results show that the more closely spaced the two spheres are, the less the specular effect dominates.

a finite difference solver capable of handling conjugate heat transfer. This interaction is described in the user's manual[3] in the following way:

RadCAD uses a stochastic integration technique (Monte Carlo) for computing radks (radiation conductors), view factors, and heating rates. Rays are emitted from each node and traced around the geometry. The rays simulate the effect of a bundle of photons. When a ray strikes another surface, energy is decremented from the ray and absorbed by the struck surface. The ray is then reflected or transmitted, according to the optical properties on the surface.

An example showing thermal desktop plots of rays is shown in Figure 13.

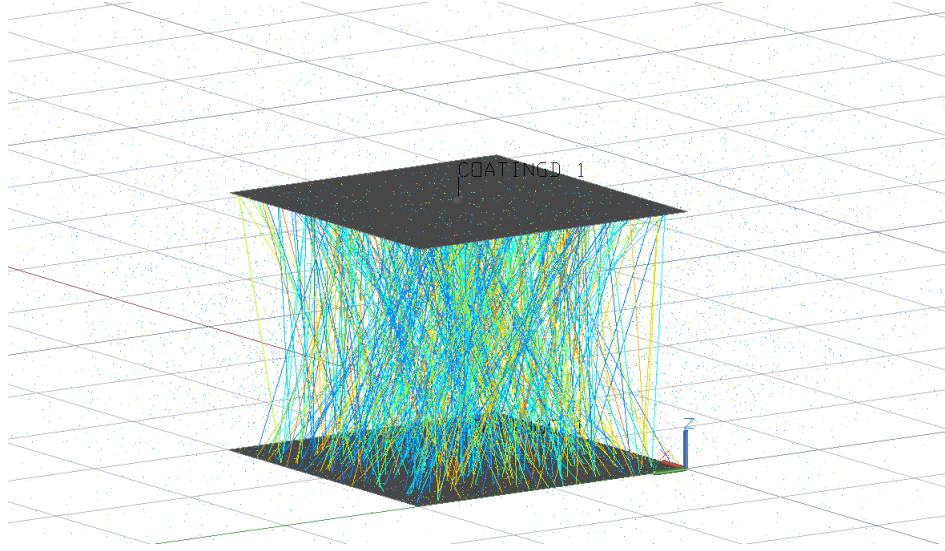


**Figure 13:** The ray is colored based on the value of its energy; red has an energy of one and dark blue has energy equal to zero. Specks (single pixels) were rays lost to the large, isothermal surroundings in this problem. Here, 200 rays from 10 radiation bands (equally spaced up to 500  $\mu\text{m}$ ), for a total of 2000 rays, are plotted.

### 3.7.2 Rays per node

The basic approach to error analysis is to estimate the variance in the mean of the sample of ray firings[3]. This variance, in conjunction with a confidence interval, may be used to generate a percentage error number[3]. The variance could either be estimated by maintaining both the sum of the energy absorbed and also the sum of the square of the energy absorbed, but this requires substantial overhead in maintaining an  $N$  by  $N$  matrix of squared energy tallies[3]. A simpler approach is to consider the ray tallies as a discrete distribution (the energy is either completely absorbed by a node or completely reflected)[3]. According to Cullimore, the discrete distribution usually gives a larger error estimate, and since this approach is simple and conservative, it's the method used in Thermal Desktop and shown in equation 17.

$$Error_{ij} = 1.65 \sqrt{\frac{1 - B_{ij}}{N_{rays} B_{ij}}} \times 100 \quad (17)$$

Cullimore goes on to say the following[3, p. 494]:

If the exact error were known, then so would the exact answer. All we can be 100% confident of is that the true answer lies between plus and minus infinity. A more practical statement of estimated error can be made using confidence intervals...the  $B_{ij}$  is the fraction of

energy that leaves node  $i$  and is absorbed by node  $j$  by all possible reflection paths. The sum of all  $B_{ij}$  for a node is equal to unity. The  $B_{ij}$  multiplied by the surface emissivity and area becomes the standard radiation conductor input to SINDA/FLUINT. A  $B_{ij}$  of one half means that node  $j$  absorbed half of the energy emitted by node  $i$ .

The error equation highlights two important facts. One is that the error is inversely proportional to the square root of the number of rays shot. The number of rays will need to be quadrupled to cut the error in half. The other is that the error depends on the magnitude of the  $B_{ij}$ . Large  $B_{ij}$  are the result of capturing a large number of emitted rays, and hence the statistical sample population is much larger than a smaller  $B_{ij}$ , yielding a lower variance and error estimate.

A simple rule of thumb in deciding the number of rays to shoot is to consider the average  $B_{ij}$  in a problem. If for a particular node, the average  $B_{ij}$  is one half, shooting 1000 rays gives an average error of about 5%. If you know that a particular radiation coupling is critical to the accuracy of the thermal simulation, say a small cryogenic surface looking at a small hot surface, then modify the error estimate based on expected values of  $B_{ij}$  for the critical component.

To get a feel for how the number of rays shot per node can affect the results, an exercise was performed. Consider two  $1\text{ m}^2$ , square, parallel plates spaced 1 m apart. The backsides of the plates are adiabatic, assume 1000 W are dissipated in one plate, the emissivities are both 0.11, and a surroundings temperature of 100K. What is the steady state result? The solution to this problem is shown in Figure 14 and Figure 15. Here, in the case where the plates are simply a 1 x 1 mesh, using the default of 5000 rays per node results in the wrong answer. The number of rays had to be increased by a factor of ten to 50,000 to obtain the correct result from Thermal Desktop. This is the inherent error in the  $B_{ij}$  as discussed before.

Are there other sources of error besides the inherent uncertainty in the stochastic integration? In fact, there are. For the next validation case, resolution was added to the panels to make them a 10 x 10 mesh. The result was an erroneous answer for the top plate of 100K (see Figure 16). This happened because the  $B_{ij}$  cutoff factor, defined as the ratio of the  $B_{ij}/F_{ij}$ , can erroneously determine rays to be inconsequential, thus truncating energy that is important to include in the solution. In other words, a radiation conductor between nodes  $i$  and  $j$  is ignored when it is less than a certain fraction of both node's radiative energy balance. When a radk has both a  $B_{ij}$  and  $B_{ji}$  less than the  $B_{ij}/F_{ij}$  cutoff factor, it is culled from the input file to speed up calculations. A good place to start is one divided by ten times the number of nodes in the radiation analysis group[3]. In the Thermal Desktop manual, Cullimore writes[3, p.509],

The estimated spread in  $B_{ij}$  for nodes in the problem must also be

considered. For example, consider the extreme case of the inside of a sphere with equal sized nodes. In this case, all  $B_{ij}$  between nodes should be exactly the same ( $1/n$ , where  $n$  is the number of nodes). A  $B_{ij}$  of zero should be used (or less than  $1/n$ ), since all  $B_{ij}$  are equally important. Picking a cutoff greater than  $1/n$  will remove all radks (ignoring variations due to statistical error). At the other extreme, for models whose temperatures are dominated by a few large nodes, a higher cutoff fraction can be deployed.

A small SINDA/FLUINT run can also be performed to verify that excessive culling has not been done. Perform a limited transient run with both a complete radk file and one that has been filtered. If the results do not differ significantly, perform the longer transient simulation with the filtered set of radks.

In this case, there were 100 nodes so a cutoff factor of 0.001 seems reasonable. However, this is the case that gave the erroneous result. Once the cutoff factor was reduced to 0.0001, the model replicated both the analytical result and the previously solved simple 1 x 1 plate Thermal Desktop model. The best practice appears to be simply setting  $B_{ij}/F_{ij}$  cutoff factor to zero (unless the run time is unacceptably long). Setting it to zero also gives the correct results and avoids any problems with culling energy.

Taking a step back, note that only one side is active on each surface. This means that the upper plate is a re-radiating surface. What if I change it's emissivity? According to theory, a re-radiating surface performs independent of emissivity<sup>13</sup>[12]. Choosing an emissivity of 0.03 instead of 0.11, with 5000 rays shot, the steady state temperature of the upper plate was 250K (a little high). When the rays shot was increased to 500,000, the average temperature of the plate was solved at 247.8K, which is again right in line with the analytical result. If the re-radiating panel's emissivity was set to blackbody, this time the average temperature of the plate was 247.2K, which is a few tenths of a degree low. It seems that emissivity does impart a small error upon the stochastic method used here.

These analysis beg the question: how many rays must be shot? Is it based on the number of nodes in the model, mostly? And what about using the progressive radiosity method instead? I can't fully answer these questions, but with this simple model, at least I can analyze this problem for this particular geometry. Here, in Figure 17, the average temperature of the plate is plotted against the number of rays shot per node.

In the next case, the same plot is shown for the 10 x 10 meshed plates (Figure 18).

Using the progressive radiosity<sup>14</sup> method on the same 10 x 10 plate meshes,

<sup>13</sup>That happens because the surface emissivity is an internal resistance and if there's no heat flow from the radiosity node to the blackbody node, then the resulting steady state temperature is not a function of emissivity.

<sup>14</sup>The progressive radiosity method only works under the gray-diffuse assumption because, at it's core, it replicates the standard thermal network analysis, solving equations via radiosi-

the plot in Figure 19 was generated. In this case, there seems to be significant variation in the result, seemingly giving less confidence in the progressive radiosity approach in terms of computer error.

### 3.8 Non-gray

Non-gray effects can significantly affect the results of some radiation heat transfer problems. For example, in his paper *Radiant heat transfer between nongray parallel plates of tungsten*, J. Robert Branstetter shows that the gray analysis can underpredict heat transfer by 5% to 25%, for the temperature differences he analyzed ranging from zero to 3200 K[1].

#### 3.8.1 Srinivasan's paradox

J. Srinivasan observed that their dewar<sup>15</sup> suffered roughly 60% more heat leak when filled with liquid nitrogen than liquid hydrogen. This counterintuitive result is explained by the wavelength and temperature dependent emissivity having decreased faster than the temperature over this interval. Though Srinivasan solved the problem analytically for only silvered surfaces, several solutions are presented here using numerical integration.

This solution begins with the Hagen-Rubens relationship, equation 18. Here,  $n$  is the refractive index,  $\kappa$  is the extinction coefficient,  $\lambda_o > 5 \mu\text{m}$ ,  $\mu_o$  is the magnetic permeability,  $c_o$  is the speed of an electromagnetic wave in vacuum, and  $r_e$  is the electrical resistivity[23, p. 123]. Note that in this equation, wavelength is expressed in units of  $[\mu\text{m}]$  and resistivity in  $[\Omega \text{cm}]$ .

$$n = \kappa = \sqrt{\frac{\lambda_o \mu_o c_o}{4\pi r_e}} = \sqrt{\frac{0.003\lambda_o}{r_e}} \quad (18)$$

With the simplification  $n = \kappa$ , the normal emissivity may be derived from electromagnetic theory, equation 19.

$$\epsilon'_n = \frac{4n}{(n+1)^2 + \kappa^2} \implies \epsilon'_{\lambda,n}(\lambda) = \frac{4n}{2n^2 + 2n + 1} = \frac{2}{n} - \frac{2}{n^2} + \frac{1}{n^3} - \frac{1}{2n^5} + \frac{1}{2n^6} - \dots \quad (19)$$

And, just like how Siegel and Howell proceed, this fraction was expanded so a simplification could be made<sup>16</sup>. The simplification is to keep only the first two terms, which is justified by observing that the index of refraction of metals is generally large at the long wavelengths being considered here ( $\lambda_o > 5 \mu\text{m}$ ).

---

ties. This tends to speed up calculations in problems where it's appropriate to make the gray-diffuse assumption.

<sup>15</sup>They describe a dewar mostly how one would expect: essentially an ideal cylindrical tank with inner and outer vessels separated by vacuum—no structural supports or other geometry.

<sup>16</sup>Siegel and Howell say this simplification isn't strictly necessary, but it was useful to conveniently setup the problem following their method.

Combining with the Hagen-Rubens relation, the Hagen-Rubens emissivity relation is derived as shown in equation 20.

$$\epsilon'_n(\lambda) = \frac{2}{\sqrt{0.003}} \sqrt{\frac{r_e}{\lambda_o}} - \frac{2}{0.003} \frac{r_e}{\lambda_o} + \dots \approx 36.5 \sqrt{\frac{r_e}{\lambda_o}} - 464 \frac{r_e}{\lambda_o} \quad (20)$$

Using the relation  $r_e \approx r_{e,273} \frac{T}{273}$ , and multiplying by 1.33 to account for hemispherical, the integral for gray parallel plates may be applied to solve the problem, as shown in equation 21.

$$q(T_1, T_2) = \int_5^{10000} \frac{E_{\lambda_b}(\lambda, T_1) - E_{\lambda_b}(\lambda, T_2)}{\frac{1}{\epsilon_h(\lambda, T_1)} + \frac{1}{\epsilon_h(\lambda, T_2)} - 1} d\lambda \quad (21)$$

Notice how the integration interval starts at 5  $\mu\text{m}$  and ends at 10 000  $\mu\text{m}$  rather than covering the entire interval from zero to infinity. The reason is because with the two term approximation, anything from zero to 5  $\mu\text{m}$  (as mentioned previously) is not being accounted for. So besides diverging at small wavelengths, this integral also diverges at very long wavelengths.

T. Echániz et al. wrote a wonderful paper called *Optical properties of metals: Infrared emissivity in the anomalous skin effect spectral region* that goes into detail on the emissivity of metals and the relationship to the anomalous skin effect, which is reported to have a large impact on results[9]. Even though this paper focuses on the anomalous skin effect, some of the concepts are similar, and they say the following (note that the equation numbers here, as well as the table and figure, refer to their paper and chart; these do not reference equations actually in this report):

Figure1 shows theoretical spectral emissivity for the classical theory (eq. 4) and for the anomalous skin effect with  $p = 1$  (eq. 6) at three temperatures. It must be noticed that the anomalous skin effect normal emissivity shows, for  $p = 1$ , a broad peak in the mid and far-infrared spectrum. Among the metals that have an anomalous skin effect behavior...only copper shows a clear experimental confirmation of an emissivity broad peak in the mid-infrared in agreement with the theoretical prediction. In the same figure, the two series expansion approximations (eq 9 and 10) are also plotted. The plots confirm the range of validity of both equations. Thus, eq 9 is a better approximation for higher temperatures, while eq. 10 works better for lower ones. In the same figure, the expansion series emissivity for  $p = 0$  is also plotted. Two facts should be outlined: on the one hand, the strong dependence of the anomalous skin effect with temperature; on the other, it is better to use the integral equation because the series expansion approach only covers a fraction of the anomalous wavelength range.

The chart this references is adapted to Figure 20 in this report.

Moving on with this restriction in mind, the solution to this problem as calculated using MathCAD is shown in Figure 21. The output for the temperature

dependent spectral emissivity is shown in Figure 22. Solutions for this problem for various metals can be found in Figures 23, 24, 25, 26, and a comparison among the metals is shown in Figure 27. The solution shows the desired 60% difference in heat transfer between the liquid nitrogen and liquid hydrogen vessels. It also shows that, because of drastic changes in non-gray spectral emissivity and absorptivity, the heat flux isn't monotonically increasing. Therefore, there exists smaller temperature differences that can actually yield the same heat flux as much larger temperature differences (this is shown by the horizontal line in the figures).

### 3.8.2 Kauder's finite non-gray parallel plates example

Lonny Kauder gave a nice example of a non-gray interaction and, as an exercise, this result was replicated on Thermal Desktop using wavelength dependent Monte Carlo ray tracing via their RadCAD module. First, consider two hypothetical coatings, coating c and coating d, with spectral reflectance as shown in Figure 28.

The data shown in Figure 28 only go to 200  $\mu\text{m}$ . This is a problem because the band fraction up to 200  $\mu\text{m}$  at 50K is only 91.5%, therefore, integration to beyond the data set is required, at least to 500  $\mu\text{m}$ . In fact, Kauder goes to 2000  $\mu\text{m}$  in his explicit solution of the plate temperature in this problem [14, p. 16]. Assuming the backs and sides of the parallel plates are adiabatic, each one has an area of 1  $\text{m}^2$ , the large, isothermal surroundings are at 0K, the plates have a 0.8m separation, and the plate with coating c has a fixed temperature of 50K. The other plate has coating d. What is the temperature of the other plate? Kauder solves this analytically [14, p. 16] and finds an answer of 34.43 K.

Using Thermal Desktop, the answer was solved as 33.48 K, which seems to further validate the Thermal Desktop non-gray calculation capability<sup>17</sup>. The solved Thermal Desktop model is shown in Figure 29.

## 4 Modeling superinsulation

### 4.1 Floating shields analytical model

The most straightforward and basic thermal model is the ideal floating shields setup. To analyze performance, consider  $N$  radiation shields between two surfaces at temperatures  $T_1$  and  $T_2$ , as shown in Figure 30. The assumptions here include steady state, gray-diffuse, and one dimensional heat transfer.

The equation for this result can be easily derived [23] and the result is shown

---

<sup>17</sup>It was necessary to use the same integration band steps as band steps in the properties definition (since the properties had to be input stepwise). After talking with the developers, it seems this bug was fixed in version 6.0 of Thermal Desktop. I was running version 5.8 at the time of this writing.

in equation 22<sup>18</sup>.

$$q = \frac{\sigma(T_1^4 - T_2^4)}{1/\epsilon_1 + 1/\epsilon_2 - 1 + \sum_{n=1}^{N-1} (1/\epsilon_{n2} + 1/\epsilon_{(n+1)1} - 1) + 1/\epsilon_{N2} + 1/\epsilon_2 - 1} \quad (22)$$

A simplified version of this equation (Figure 31) was used to solve the case for ten layers of insulation from 220K to 90K. Since this is an analytical equation, once the heat flux is known, it's possible to solve for the temperature profile. This is shown in Figure 32.

## 4.2 Semi-empirical models

Ever since the invention of superinsulation by Sir James Dewar [8], researchers have made progress modeling the heat transfer processes manifesting in the geometry of closely spaced layers of thin, highly reflecting materials, but the problem has never been perfectly solved, as has been discussed throughout the theory section of this report. Nevertheless, over the years, there's been many attempts to solve the heat transfer problem of superinsulation. To date, no perfect generalized model exists. That's because there's many different ways to configure the insulation—each way more or less difficult, analytically. The strong interplay between radiation and conduction has foiled most attempts at generalization. For example, the random influence of contacting spacer layers makes a solution hard to come by. Making matters worse are the advanced physics effects previously discussed several times.

Today, for back of the envelope calculations, engineers use several formulations for modeling the heat transfer through superinsulation. One of the more popular forms of modeling consists of semi-empirical models. By their nature, since the energy equation is never actually solved, the temperature gradient through the blanket cannot be derived from the semi-empirical models. Nevertheless, they can be useful to approximate the heat flow.

It seems the most popular semi-empirical model came out of a 1969 AIAA conference publication by Cunningham and Tien[5], and they re-published this work again[6], partly funded by NASA Glenn Research Center, which, at that time, was known as Lewis Research Center. Some of their more comprehensive works include *Cryogenic Insulation Heat Transfer*[26], *Thermal performance of multilayer insulations* [4][15], and a chapter from the book edited by Jerry T. Bevan's, *Thermophysics: Applications to Thermal Design of Spacecraft*[7].

Herein, the derivation of Cunningham and Tien's semi-empirical model is reproduced primarily<sup>19</sup> from Bevan's book. The reason is two sided: not only to marvel at the usefulness of the equation, but also explore the weaknesses in

<sup>18</sup>This equation can be further simplified if all the shields have the same emissivity, and again even further simplified if the outer walls also have the same emissivity.

<sup>19</sup>It is useful for the interested reader to look at all of Cunningham and Tien's publications since each of them contains slightly different information on the progression of how to develop this model.



this approach. Besides, the original authors skip many steps and it was never given an academic, clear treatment in text.

First, some assumptions must be granted, but more are added later as needed.

1. optically thick layers (no quantum tunneling) |  $\tau \ll 1$
2. one dimensional heat transfer
3. isothermal layers
4. neglect gas conduction / convection
5. separable radiation and conduction terms
6. steady state
7. infinite plane geometry
8. neglect directionality of emission
9. no internal heat generation
10. diffuse-gray
11. thin film (neglect conduction through the layer)
12. no seams or other kinds of disturbances

Regarding the first assumption, some researchers, such as T. Ohmori<sup>20</sup>, A. Yamamoto<sup>21</sup>, and M. Nakajima[19], as well as R.P. Shutt have found that thin vapor deposited aluminumized layers, on the order of 300Å to 900Å, exhibit some transmissivity. Tuttle found that long-wavelength radiation at low temperatures can penetrate the layer through a quantum tunneling effect.

This quantum effect ought to occur when the wavelength of radiation is on the order of the same size as the layer spacing. A typical layer spacing for superinsulation might be ten layers per centimeter<sup>22</sup>

Cunnington and Tien approximate the heat transfer between two layers (Figure 33) by invoking the separable assumption as shown in equation 23<sup>23</sup>. The separable assumption isn't particularly strong because clearly conduction and radiation are tightly coupled in this geometry. Nevertheless, this approximation drastically simplifies the approach.

$$q = \frac{k(T_1 - T_2)}{l} + \frac{E_{b1} - E_{b2}}{1/\epsilon_1 + 1/\epsilon_2 - 1 + 3/4\tau} \quad (23)$$

---

<sup>20</sup>Ishikawajima-Harima Heavy Industries Co. Ltd.

<sup>21</sup>High Energy Accelerator Research Organization

<sup>22</sup>Fifteen layers per centimeter is often cited, however, this depends on the spacer used.

<sup>23</sup>Usually the heat flux variable  $q$  is written with a dot above (to indicate energy *per second*) and two primes to indicate that it's a flux (*per area*), but here it's just written as  $q$  to simplify text output

Here, the transmissivity was included for parallel plates, but this term goes to zero because the film is assumed to be optically thick. Then the equation can be simplified as shown in equation 24. Here,  $k$  is the thermal conductivity of the spacer.

$$q = \frac{k(T_1 - T_2)}{l} + \frac{\epsilon_1 \epsilon_2}{\epsilon_1 + \epsilon_2} (E_{b1} - E_{b2}) \quad (24)$$

According to the approach they took in the Bevens book, for  $n > 1$ ,  $E_{b1} = n^2 \sigma T_1^4$  and  $\epsilon = n \bar{\epsilon}(T)$  where  $n$  is the index of refraction (assumed to be 1 for crinkled layers and 1.14 for thin, fibrous spacers) and  $\bar{\epsilon}(T)$  is the total, hemispherical emissivity. With this substitution, equation 25 is obtained.

$$q = \frac{k(T_1 - T_2)}{l} + \frac{\bar{\epsilon}_1 \bar{\epsilon}_2}{\bar{\epsilon}_1 + \bar{\epsilon}_2} (n^3 \sigma (T_1^4 - T_2^4)) \quad (25)$$

Now, the authors wanted to include a pressure dependency in the conduction term so, referencing his own work *A correlation for thermal contact conductance of nominally flat surfaces*[25], he uses the following relationship (equation 26) for a single or double interface where  $k_s$  is the spacer conductivity,  $p$  is the loading areal pressure,  $E$  is the modulus of elasticity,  $N_c$  is the number of contacts (one for embossed or crinkled insulation, and two for netting),  $c$  is the empirical constant, and (an empirical constant)  $d$  is roughly equal to 1/2.

$$k \equiv \frac{Hl}{N_c} \approx \frac{k_s c p^d}{E} \frac{l}{N_c} \quad (26)$$

But Cunningham and Tien didn't want to worry about  $k_s$ ,  $E$ , or the constant, so they instead lumps them into another parameter  $c_T \approx K_s c / E$ . Now the problem is how to apply this single contact semi-empirical equation to many contacts. So they assume that the following relationship holds (equation 27) where  $N$  is the number of one shield one spacer segments and  $l$  is the spacer thickness.

$$k \equiv \frac{c_T p^d l}{N} \quad (27)$$

Then the equation reduces to the form shown in equation 28.

$$q = \frac{c_T p^d l}{N} \frac{(T_1 - T_2)}{l} + \frac{\bar{\epsilon}_1 \bar{\epsilon}_2}{\bar{\epsilon}_1 + \bar{\epsilon}_2} n^3 \sigma (T_1^4 - T_2^4) \quad (28)$$

Now, they assume double sided, thin insulation such that  $\bar{\epsilon}_1(T) = \bar{\epsilon}_2(T)$  and now they invoke a particularly weak assumption. They assume the interlayer change in temperature is small and justifies this by assuming many shields. The intention is to set up the model essentially for a continuum assumption such that  $x_{tot} = N_o h$  and letting  $x \rightarrow 0$  the result reduces to the form shown in equation 29.

$$q = \frac{c_T p^d l}{N} \frac{\Delta T}{l} + \frac{\bar{\epsilon}(T)}{2} (n^3 \sigma l) \frac{\Delta T^4}{l} \quad (29)$$

By analogy of the continuum, Cunningham and Tien argues that, in the limit of the continuum,  $\Delta T \rightarrow dT$  and  $l \rightarrow dx$ , and now the ordinary differential equation is apparent (equation 30).

$$q = \frac{c_T p^d l}{N} \frac{dT}{dx} + \frac{\bar{\epsilon}(T)}{2} (n^3 \sigma l) \frac{d(T^4)}{dx} \quad (30)$$

Then, assuming  $\beta \equiv T^4$ , the chain rule implies that  $d(T^4)/dx = 4T^3 dT/dx$ . At this point, the heat transfer relation is shown in equation 31.

$$q = \frac{c_T p^d l}{N} \frac{dT}{dx} + 2\bar{\epsilon}(T) n^3 \sigma l T^3 \frac{dT}{dx} \quad (31)$$

We've made progress with some ambitious assumptions by reducing this problem to a continuous, one dimensional model that is essentially in a form analogous with Fourier's law. It can be thought of as a hybrid separated mode and radiation diffusion model. At this point, Cunningham and Tien admit that they still don't like the form of their contact conductance law, therefore, they modify it again so that they may proceed in the solution such that  $c_T \equiv k_s c/E = ck_s(T)/E(T) \equiv b_1 T^{\alpha_1}$ . They also assume that the total, hemispherical emissivity is appropriate and follows a form of  $\bar{\epsilon}(T) = b_2 T^{\alpha_2}$ . Here,  $b_1$ ,  $b_2$ ,  $\alpha_1$ , and  $\alpha_2$  are constants. The authors write,

Total, hemispherical emittance as a function of temperature for aluminum surfaces...excellent agreement is found with the form  $\bar{\epsilon} = b_2 T^{2/3}$  over the major portion of temperature useful to cryogenics[7, p.118].

Cunningham and Tien report that for 400Å to 500Å aluminum on mylar, the total, hemispherical emittances as  $\epsilon = (6.45 \times 10^{-4} K^{-2/3}) T^{2/3}$ , whereas for aluminum foil, they report  $\epsilon = (6.05 \times 10^{-4} K^{-2/3}) T^{2/3}$ . For a comparison, the *Spacecraft thermal control handbook* reports  $\epsilon = (4.40 \times 10^{-4} R^{-2/3}) T^{2/3}$  and  $\epsilon = (3.88 \times 10^{-4} R^{-2/3}) T^{2/3}$ —taking the mean and converting to Kelvin, the result is  $6.1 \times 10^{-4} K^{-2/3}$  which is right in line with Cunningham and Tien's original measurements<sup>24</sup>. So now we have equation 32.

$$q = \left( \frac{b_1 T^{\alpha_1} p^d l}{N} + 2b_2 T^{\alpha_2} n^3 \sigma l T^3 \right) \frac{dT}{dx} \quad (32)$$

Strictly by analogy, we assume this behaves like the one-dimensional Fourier law  $q = k_{rad+cond}(T, P, N) dt/dx$ . It's useful to review where this comes from:  $d/dx(k(T)dT/dx) = 0$  such that with the product rule,

$$\frac{dk}{dx} \frac{dT}{dx} + k(T) \frac{d^2 T}{dx^2} \quad (33)$$

---

<sup>24</sup>For the curious reader who has seen the final equation before, note that this is where the 4.67 exponent comes from. Also, note that there is more development that makes finding  $b_1$  irrelevant, besides that,  $\alpha_1 \equiv 1$  to a first approximation.

So in order to reduce this to the aforementioned form, one must assume the combined thermal conductivity is constant such that  $dk/dx = 0$ . This leaves  $k(T, P, N)d^2T/dx^2 = 0$ .

Now, obviously, the thermal conductivity is strongly temperature dependent in the cryogenic regime. Nevertheless, in order to proceed with this ordinary differential equation solution, this assumption must be made. The result is an equation that is linear being used to describe a non-linear scenario. This failure is ultimately why the Cunningham and Tien model only has correlative use as opposed to full predictive potential for insulations that have yet to be constructed. Because this equation is only good after having been correlated in a test. So, after integration from 0 to  $N_o h$ , which is approximately zero to the thickness of the blanket, equation 34 results.

$$q = \frac{b_1 p^d l}{N N_o h} \frac{T_h^{\alpha_1+1} - T_c^{\alpha_1+1}}{\alpha_1 + 1} + 2b_2 n^3 \sigma l \frac{T_h^{\alpha_1+4} - T_c^{\alpha_1+4}}{\alpha_2 + 4} \quad (34)$$

At this point, Cunningham and Tien lament that  $b_1$  and  $\alpha_1$  are hard to evaluate. So as a first approximation we assume  $\alpha_1 = 1$  and  $b_1 = \text{constant}$  and because the layers are thin, it is assumed  $l = h$ , and if  $c' \equiv b_1/N_o$  and  $T_m \equiv (T_h + T_c)/2$ , then equation 35 is obtained.

$$q = \frac{c' p^d T_m}{N} (T_h - T_c) + \frac{3}{7} \frac{b_2 n^3 \sigma}{N_o} (T_h^{14/3} - T_c^{14/3}) \quad (35)$$

Again, at this point, Cunningham and Tien ran into a problem. In their data, they had trouble correlating this equation so it could predict the heat flux for different pressures. So, instead, they fit to layer density. This probably caused confusion because, for Cunningham and Tien, layer density arose due to pressure effects. It is not a controlled parameter, as it were. Yet, later, engineers tried to use this expression to find an optimal layer density, but this is equivalent to trying to find an optimal loading pressure on the insulation. Next, how they develop the equation in terms of layer density is shown.

Assuming  $\bar{N} = (p/a)^{1/n}$  where  $\bar{N} = N_o/t$  is the layer density and  $a$  and  $n$  are constants and  $t$  is the blanket thickness. Then, examine this substitution:

$$\frac{c' p^d T_m}{N} (T_h - T_c) = \frac{c' (a \bar{N}^n)^d T_m}{N} (T_h - T_c) \quad (36)$$

And assuming the number of shields equals the number of layer space segments such that  $N = N_o$  and defining  $m \equiv nd - 1$  and  $c'' \equiv c' a^d$  then

$$= \frac{c'' \bar{N}^m}{t} T_m (T_h - T_c) \quad (37)$$

The final equation reported by Cunningham and Tien is thus equation 38. They fit this equation to test data by adjusting  $c''$ ,  $m$ , and  $b_2$ . To do this, they

write that they first subtract the radiative flux and then plot the difference times thickness as a function of layer density.

$$q = \frac{c''}{t} \bar{N}^m T_m (T_h - T_c) + \frac{3}{7} \frac{b_2 n^3 \sigma}{N_o} (T_h^{14/3} - T_c^{14/3}) \quad (38)$$

#### 4.2.1 Krishnaprakas's comparison

Previously, the Cunningham and Tien model was discussed. It uses no fewer than twenty two assumptions. It's telling that in C.K. Krishnapraka's work, *Heat transfer correlations for multilayer insulation systems*, they show that a model of form,

$$q = h(T_h - T_c) + \epsilon'_{eff} \sigma (T_h^4 - T_c^4) \quad (39)$$

is at least as accurate as the Cunningham-Tien form,

$$q = c_1(T_h^2 - T_c^2) + c_2(T_h^4 .67 - T_c^4 .67) \quad (40)$$

And in Keller and Cunningham's *Thermal performance of multilayer insulations*, the author writes that an equation of the form,

$$q = c_3(T_h^2 - T_c^2) + c_4(T_h^3 - T_c^3) + c_5(T_h^4 .67 - T_c^4 .67) \quad (41)$$

is more accurate than a form without the  $T^3$  term[16, p.4-24]. So it seems that this kind of polynomial fit simply tends to work well, and, perhaps, to use such an equation, the previously mentioned complex derivation is not necessary. Nevertheless, this is not a criticism of Cunningham and Tien's work. Without their massive contributions to this field, much less would be known about heat transfer through superinsulations. After all, to suggest this was their only contribution would be a great oversimplification of the body of their work.

#### 4.2.2 Iterative separated mode model

Another notable model includes the separated mode iterative model, discussed by McIntosh[18]. This formulation works by assuming a temperature profile and then adjusting it until the heat transfer between each layer converges. A block diagram of how this program works is shown in Figure 34.

#### 4.2.3 Seams and cracks in superinsulation

There seems to be a lack of research in this area, which motivated this study. There are three notable research papers on this topic.

The first notable study was the work done at the Jet Propulsion Laboratory for the Cassini program. Here, twenty layer test blankets with dacron net separators were instrumented to measure temperature drops through the blanket at various locations. The results showed that the radiative heat loss from the room-temperature test article to the LN2 cooled chamber wall varied by an

order of magnitude, from less than  $3W/m^2$  to almost  $30W/m^2$ , depending on distance from the seam[11][17]. These results are shown in Figure 35.

The other two notable papers were by the same author, Q.S. Shu at the Fermi National Accelerator Laboratory. Here, an analytical *enhanced black cavity model* was developed to explain the unexpectedly large heat flux through a crack (or slot) in multilayer insulation. Shu reported an increase in heat load due to unit crack area above a hundred times the heat flux of a blanket without cracks. The setup and solution are shown in Figures 36 and 37, respectively.

In the conclusion, Shu wrote[22],

1. a crack in a MLI blanket will cause a significant increase in the heat flux. The mean equivalent thermal conductivity of a narrow crack is 3-8 W/m/K. The increase in heat flux due to unit crack area is a function of the aspect ratio of the crack with a maximum of 149 W/m/m.
2. the use of aluminized mylar patches to cover the crack at each layer is good but may not be easy to install, however, the use of flat patches on a few layers will give almost the same improvement as patches between each layer. Placing the patches in the outer (warmer) half of the blanket is much better than in the inner (colder) half. Putting patches on the outside of the crack is not very effective;
3. Mylar with more aluminizing is better as a patch material...
4. reducing the emissivity of the cold surface under a narrow crack does not significantly effect the heat flux
5. the presence of cracks and patches changes the temperature distribution in the blanket near the cracks. The layer closest to the cold surface increased and that of the layer closest to the warm surfaces decreased as the width of the slots increased...
6. the local equivalent thermal conductivity of a crack is a sensitive function of the distribution and number of patches along the crack
7. the experimetnal results are generally in agreement with the enhanced black cavity model

To date, no one has attempted to verify these results with their own experiment, which is unfortunate. Since a spherical geometry was of interest in this particular thesis, Shu's work is not validated here either.

#### 4.2.4 Other models

There are numerous models reported in the literature—too many to comment on here. One of the best summaries of this information is in *Multilayer insulation: a state of the art assessment*[2] by Richard W. Cartwright<sup>25</sup>, so the curious reader with access ought to check out this resource.

<sup>25</sup>This document is available by request only through the Chemical Propulsion Information Analysis Center at the Johns Hopkins University, Whiting School of Engineering and reproduction is not authorized.

#### 4.2.5 Other topics

There are many other topics left unexplored, including all of the intricacies and peculiarities associated with meeting requirements and physical construction. The interested reader is encouraged to explore the *Spacecraft thermal control handbook* for more information on these topics.

## 5 Material Properties

It was important to pick an optical property that refers to an optically thick layer. Also, the gray assumption must be deployed because the data for temperature dependent spectral emissivity was not readily available at the time of this analysis.

The optical property chosen for the insulation then was that of aluminized kapton of 1 mil thickness (beginning of life<sup>26</sup>)[11]. The reported value for the infrared emissivity is 0.61, which seems a little large, but it's in the range of the other aluminized films. Lower values can be approached (such as with aluminum tape), but these materials aren't typically used for insulation layers.

Regarding physics properties, for the layers of insulation, polyimide (kapton) was chosen[11].

## 6 Geometry

A spherical geometry has two advantages, the biggest being the elimination of edge effects, the other being that often cryogenic tanks take the shape of a sphere. The area was set to  $1m^2$  (primarily so that heat flux was numerically equivalent to the total heat transferred through each submodel)<sup>27</sup>.

$$A = 1m^2 \quad (42)$$

$$r = \sqrt{1m^2/4\pi} \approx 0.282m \quad (43)$$

Layer thickness was assumed to be  $2.5 \times 10^{-5}m$  and ten layers of insulation were consistently used throughout the solutions reported herein. Layer spacing was  $1mm$ . Lateral conduction and conduction through the thickness of the layers are solved as part of the SINDA finite difference solution.

---

<sup>26</sup>Insulations exposed to different environments suffer changes in their optical properties. Due to time constraints, these effects are not explored in this paper. Other unexplored topics include gas conduction, as well as lateral conduction, and the way insulation responds to penetrations such as piping, or perforations to allow for venting. Superinsulation is a deep, complex subject, and probably deserves a textbook of its own.

<sup>27</sup>Each layer was given it's own submodel to simplify the SUBMAP function which tracks heat moving from one submodel to another.

## 7 Boundary conditions

This is a simple approach. There are two Dirichlet conditions, one for the innermost surface and one for the outermost surface. These temperatures were fixed at 90 K and 220 K. After validation cases are performed, the surroundings are brought closer to the outer layer, and various seam sizes are explored, as well as the effect of an increasing contact conductance for this specific geometry (ten layer, spherical blanket).

## 8 Validation Cases

The algorithm utilized for heat transfer calculations by radiation is Monte Carlo ray tracing. As previously discussed, this is called the RadCAD plug-in, by the developers of Thermal Desktop, C & R Technologies [3].

### 8.1 Optimizing rays per node and Bij/Fij cutoff factor

The first few cases ran were to decide what a good number of rays were, as well as the impact of the cutoff factor. This particular case was using perfectly black surfaces on the inner and outer boundaries, the outer boundary being large, isothermal surroundings<sup>28</sup>. For all cases, the inner temperature is 90K and the outer temperature 220K. The results are shown in Figure 38. Here, each layer used a 10 x 10 mesh. It seems that for this geometry, at least 100,000 rays are necessary with a cutoff factor of zero. Because the workstation processing these results is powerful<sup>29</sup>, the number of rays for future cases will actually be 1,000,000.

### 8.2 Comparison to floating shields ideal solution

Next, to validate Thermal Desktop, a similar case was solved. This time, the outer boundary was brought very close—to the spacing of the insulation layers—and the inner and outer boundary emissivities were set to match the layer emissivities at 0.61, as previously discussed. The comparison between the two solutions is shown in Figure 39. The agreement is satisfactory. It seems slight deviations from perfection result from the random and numerical nature of the Monte Carlo solution. The total heat flux was  $-5.34W/m^2$ <sup>30</sup>, which compares to  $-5.15W/m^2$  in the analytical solution. The relative error, shown in equation 44, is acceptable for the purposes of this study. With confidence, more interesting cases can now be solved.

---

<sup>28</sup>Note that here the area was accidentally set to  $4m^2$ , resulting in the increased heat leak on the order of  $22W$ . This should not impact the number of rays shot, since that is a symmetrical effect.

<sup>29</sup>This machine has an eight core Intel Xeon CPU E5-1630 v4 at 3.70GHz with 32 GB DRAM and an NVIDIA Quadro M5000 graphics card

<sup>30</sup>The negative sign simply results from taking the result from the sink node, which is the cold boundary node



$$Err = \frac{5.34 - 5.15}{5.15} 100 \approx 3.7\% \quad (44)$$

### 8.3 Case 1: Floating shields, 3° crack, large isothermal surroundings, gray-diffuse

This time, the geometry was modified to create a 3° crack in one half of the insulation. The nodalization was adjusted such that more nodes were located closer to the crack—something that remains consistent in the rest of the analysis. The solved heat flux was  $-6.04W/m^2$  which represents roughly a 13% increase in total heat flux from the case with no crack. This is quite large, given the fact that we’re only considering a 3° opening over half of the sphere. The solved temperature profile and results are shown in Figures 40, 41, 42, 43, 44, 45, 46, 47, 48, 49, 50.

### 8.4 Case 2: Floating shields, 3° crack, large isothermal surroundings, gray with directional emission

In this case, the effect of directional emission<sup>31</sup>[14] bouncing out of the seam are explored. This is the great advantage of Thermal Desktop—cases like this, which are incredibly difficult analytically, can be solved with just a few more clicks. In this case, reflections are assumed to be diffuse.

The result was a total heat flux of  $-6.13W/m^2$ , which is just 1.5% greater than the case without directional emission. This is within the uncertainty of the Monte Carlo approach and the results are very similar to case 1, so they are not reported herein<sup>32</sup>. It seems directional emission may be safely ignored in cryogenic insulation in this temperature regime.

### 8.5 Case 3: Floating shields, 3° crack, large isothermal surroundings, gray with directional emission and specular (mirrorlike) reflections

This time specular, mirrorlike reflections are added to the analysis. This only increased the heat leak to  $-6.17W/m^2$ , which is small enough to be safely ignored. It seems the specular effects may be disregarded for cracks in insulation.

### 8.6 Case 4: Floating shields, 6° crack, large isothermal surroundings, gray-diffuse

In this case, the solved heat leak was  $-6.70W/m^2$ . This is a 25% increase from the ideal case without a crack. The solved temperature profile and results are shown in Figures 51, 52, 53, 54, 55, 56, 57, 58, 59, 60, 61.

<sup>31</sup>Here, the same directional emissivity curve is used for general metallic surfaces as published by Kauder and discussed earlier in this report.

<sup>32</sup>The goal is literally to save paper on printouts, nothing interesting is revealed by this case

### 8.7 Case 5: Floating shields, 12° crack, large isothermal surroundings, gray-diffuse

In this case, the solved heat leak was  $-7.95W/m^2$ . This is a 49% increase from the ideal case without a crack. The solved temperature profile and results are shown in Figures 62, 63, 64, 65, 66, 67, 68, 69, 70, 71, 72.

### 8.8 Case 6: Floating shields, 3° crack, surroundings brought very close, gray-diffuse

In case 6, the surroundings were brought within 1 mm of the outermost layer with an emissivity equivalent to the rest of the emissivities in the system: 0.61. The resulting heat leak was  $-5.78W/m^2$  which is relatively close to the ideal, floating shields with no cracks case. The temperature profile is shown in Figure 73.

### 8.9 Case 7: Contacting shields, 3° crack, large, isothermal surroundings, gray-diffuse

In case 7, a contact conductance of  $0.05W/m^2/K$  was applied between each layer of insulation<sup>33</sup>. This case is a bit more realistic. The resulting heat leak was  $-6.66W/m^2$  and the temperature profile is shown in Figure 74, and the graphical results are shown in Figures 75, 76, 77, 78, 79, 80, 81, 82, 83, 84.

### 8.10 Case 8: Contacting shields, stronger contact, 3° crack, large, isothermal surroundings, gray-diffuse

This time, the effect of increasing the contacting conductance by an order of magnitude to  $0.5W/m^2/K$  is considered. The heat leak was drastically increased to  $-11.97W/m^2$ . This shows the powerful impact of contact conductance as layers are more forcefully pressed together. Also, temperature gradients become more shallow as the dominance of the effect of the crack on the heat leak is dwarfed by the effect of the contact conductance. The temperature profile is shown in Figure 85, and the graphical results shown in Figures 86, 87, 88, 89, 90, 91, 92, 93, 94, 95.

### 8.11 Non-gray case

How does a gray blanket compare to a blanket with the non-gray assumption? To find out, a ten layer blanket case was created for a cylindrical geometry. The temperatures ranged from 20 K on the cold side to 220 K on the hot side. The gray case assumed an emissivity of 0.03, which, according to the Hagen-Rubens two term approximation, is the room temperature value of aluminum at roughly infrared wavelengths. This resulted in the temperature profiles and plot shown

---

<sup>33</sup>Because I'm not entirely sure what contact conductance is reasonable, another case is solved for a contact conductance ten times greater in case 8.

in Figure 96. Here, the gray case performs worse because the emissivity tends to fall with decreasing temperature, which isn't accounted for in the gray case. It turns out in this case that the ratio of heat leak works out to be a factor of 0.586, which means assuming gray is a bit conservative from the perspective of radiation heat transfer.

## 9 Discussion

The floating shields case suffered a heat leak of  $-5.34W/m^2$ , compared to  $-6.04W/m^2$  in the case with a  $3^\circ$  crack,  $-6.7W/m^2$  in the case with a  $6^\circ$  crack, and  $-7.95W/m^2$  in the case with a  $12^\circ$  crack. Directional emissivity and specular, mirrorlike reflections may be ignored. Contact conductance was shown to have a significant effect on the solution.

The average heat flux due to the seam appears to decrease with increasing aspect ratio, as shown in Figure 97. To explain this, it's hypothesized that the smaller aspect ratios behave more nearly to a blackbody cavity.

In addition, patches were found to be a very effective means of reducing the increased heat leak due to the seams.

## List of Figures

1	A schematic of a cross section of superinsulation, adapted from NASA [10]. . . . .	4
2	The famous Plank blackbody distribution, showing the emission spectrum for some blackbody at a temperature of 20K. This curve will shift to the left as the temperature of the blackbody increases. . . . .	6
3	A computer algebra system, like MathCAD, is very useful to avoid the table lookup typically associated with band fractions. . . . .	8
4	Directional emissivity curve for a dielectric with an index of refraction of $n = 1.5$ [14] . . . . .	9
5	Directional emissivity curve for a conductor with an index of refraction of $n=5.7+i9.7$ [14] . . . . .	10
6	This relationship, derived from electromagnetic theory for a hypothetical ideal conductor, is where the often cited guideline that hemispherical emissivity is 1.3 times the normal emissivity originates [14]. . . . .	11
7	Ratio of hemispherical to normal emissivity for emission into air [13]. . . . .	12
8	Radiation heat transfer between concentric cylinders . . . . .	13
9	As the outer sphere tends towards a blackbody condition, the heat transfer is increased. . . . .	13
10	Some paths, like path B, won't reflect back to the opposing surface. . . . .	15
11	Concentric specular sphere heat transfer example showing the boundary conditions. The effect of different emissivities is evaluated, as well as the effect of a changing annulus size. . . . .	16

12	These results show that the more closely spaced the two spheres are, the less the specular effect dominates. . . . .	17
13	The ray is colored based on the value of its energy; red has an energy of one and dark blue has energy equal to zero. Specks (single pixels) were rays lost to the large, isothermal surroundings in this problem. Here, 200 rays from 10 radiation bands (equally spaced up to 500 $\mu\text{m}$ ), for a total of 2000 rays, are plotted. . . . .	18
14	A radiation network and the radiosity method is used to solve this basic heat transfer problem. . . . .	41
15	This figure shows the result of the solution from this problem, as well as the associated Thermal Desktop results. . . . .	42
16	In this case, the Bij cutoff factor was set too low for the number of nodes and rays being shot, therefore, many of the rays (having failed the Bij/Fij) were neglected from the resultant, leading to a lower predicted temperature. . . . .	43
17	Variation in the plate node average temperature settles, in this case, once 300,000 rays per node are shot (1 x 1 plate mesh case). There is an interesting jump near 100,000 rays per node that is hard to explain. . . . .	43
18	Variation in the plate node average temperature settles, in this case, once 100,000 rays per node are shot (10 x 10 plate mesh case). . . . .	44
19	Variation in the plate node average temperature settles, in this case, once 100,000 rays per node are shot (10 x 10 plate mesh case using the progressive radiosity method, as opposed to the Monte Carlo method used in all other cases). . . . .	44
20	Figure by T. Echániz et al. [9]. . . . .	45
21	Solution to the nongray dewar problem following the approach of Srinivasan [24] which keeps a two term approximation of the Hagen-Rubens relation. . . . .	46
22	Predicted temperature dependent spectral emissivities as calculated with the two term Hagen-Rubens approximation. . . . .	47
23	Solution to Srinivasan's problem for a dewar with both surfaces coated with silver. . . . .	48
24	Solution to Srinivasan's problem for a dewar with both surfaces coated with aluminum. . . . .	49
25	Solution to Srinivasan's problem for a dewar with both surfaces coated with copper. . . . .	50
26	Solution to Srinivasan's problem for a dewar with both surfaces coated with platinum. . . . .	51
27	The comparison shows that platinum performs relatively poorly compared to silver and copper. Gold and aluminum seem to perform slightly worse according to the two term Hagen-Rubens non-gray approximation. . . . .	52

28	Kauder gave spectral plots for the two hypothetical coatings used in his example, note that the units are micrometer on the x-axis. Note that when trying to match these results in Thermal Desktop, it was necessary to assume this chart shows the spectral emissivity as opposed to the spectral reflectance. It seems the figure was mislabeled. . . . .	52
29	The solution to Kauder's example as performed using Thermal Desktop. Kauder reveals the analytical solution to two finite non-gray square plates in his analysis[14]. . . . .	53
30	Radiation shields between concentric cylinders or spheres [23]. . .	53
31	The basic ideal shields solution. The histogram shows how much the total heat leak is reduced by adding additional layers. . . . .	54
32	The solved temperature profile for the ideal, floating shields case with ten layers. . . . .	54
33	Schematic showing the starting point of the Cunningham and Tien analysis—simply two layers of insulation and their properties. Note that the temperature is assumed to exist but isn't known or prescribed. . . . .	55
34	A block diagram for a iterative separated mode superinsulation model. . . . .	55
35	Results of the Cassini program study on multilayer blanket performance[17].	56
36	Schematic of the geometry Shu analyzed in his 1987 study[21]. .	56
37	Results from Shu's 1987 study[21]. . . . .	57
38	It seems a minimum of 100,000 rays with a cutoff factor of zero is acceptable for this particular geometry (case six). . . . .	58
39	The Thermal Desktop solution for this test case of floating shields has satisfactory agreement. . . . .	58
40	Temperature profile with maximum and minimum temperature nodes being shown for case 1. . . . .	59
41	Case 1, layer 1. . . . .	60
42	Case 1, layer 2. . . . .	60
43	Case 1, layer 3. . . . .	61
44	Case 1, layer 4. . . . .	61
45	Case 1, layer 5. . . . .	62
46	Case 1, layer 6. . . . .	62
47	Case 1, layer 7. . . . .	63
48	Case 1, layer 8. . . . .	63
49	Case 1, layer 9. . . . .	64
50	Case 1, layer 10. . . . .	64
51	Temperature profile with maximum and minimum temperature nodes being shown for case 4. . . . .	65
52	Case 4, layer 1. . . . .	66
53	Case 4, layer 2. . . . .	66
54	Case 4, layer 3. . . . .	67
55	Case 4, layer 4. . . . .	67
56	Case 4, layer 5. . . . .	68

57	Case 4, layer 6. . . . .	68
58	Case 4, layer 7. . . . .	69
59	Case 4, layer 8. . . . .	69
60	Case 4, layer 9. . . . .	70
61	Case 4, layer 10. . . . .	70
62	Temperature profile with maximum and minimum temperature nodes being shown for case 5. . . . .	71
63	Case 5, layer 1. . . . .	72
64	Case 5, layer 2. . . . .	72
65	Case 5, layer 3. . . . .	73
66	Case 5, layer 4. . . . .	73
67	Case 5, layer 5. . . . .	74
68	Case 5, layer 6. . . . .	74
69	Case 5, layer 7. . . . .	75
70	Case 5, layer 8. . . . .	75
71	Case 5, layer 9. . . . .	76
72	Case 5, layer 10. . . . .	76
73	Temperature profile with maximum and minimum temperature nodes being shown for case 6. . . . .	77
74	Temperature profile with maximum and minimum temperature nodes being shown for case 7. . . . .	78
75	Case 7, layer 1. . . . .	79
76	Case 7, layer 2. . . . .	79
77	Case 7, layer 3. . . . .	80
78	Case 7, layer 4. . . . .	80
79	Case 7, layer 5. . . . .	81
80	Case 7, layer 6. . . . .	81
81	Case 7, layer 7. . . . .	82
82	Case 7, layer 8. . . . .	82
83	Case 7, layer 9. . . . .	83
84	Case 7, layer 10. . . . .	83
85	Temperature profile with maximum and minimum temperature nodes being shown for case 7. . . . .	84
86	Case 8, layer 1. . . . .	85
87	Case 8, layer 2. . . . .	85
88	Case 8, layer 3. . . . .	86
89	Case 8, layer 4. . . . .	86
90	Case 8, layer 5. . . . .	87
91	Case 8, layer 6. . . . .	87
92	Case 8, layer 7. . . . .	88
93	Case 8, layer 8. . . . .	88
94	Case 8, layer 9. . . . .	89
95	Case 8, layer 10. . . . .	89
96	Cylinder gray vs non-gray . . . . .	90
97	Cylinder gray vs non-gray . . . . .	90

## References

- [1] J. Robert Branstetter. Radiant heat transfer between nongray parallel plates of tungsten. Technical report, 1961. Technical Note D-1088.
- [2] Richard V. Cartwright. Multilayer insulations: a state of the art assessment. Technical report, 2011. Johns Hopkins University, Whiting School of Engineering.
- [3] Brent Cullimore and Steven G. Ring et al. Thermal desktop user’s manual. Technical Report Version 5.8, C & R Technologies, Jun 2015. CAD Based Thermal Analysis and Design.
- [4] G.R. Cunningham, C.W. Keller, and G.A. Bell. Thermal performance of multilayer insulations. Technical Report NASA-CR-72605 & LMSC-A903316, Lockheed Missiles and Space Co., Apr 1971. Sunnyvale, Calif.
- [5] G.R. Cunningham and C.L. Tien. A study of heat-transfer process in multilayer insulations. Number 69-607, San Francisco, California, June 1969. AIAA 4th Thermophysics Conference, Lockheed Palo Alto Research Laboratory.
- [6] G.R. Cunningham and C.L. Tien. A study of heat-transfer process in multilayer insulations. *AIAA Progress in Astronautics and Aeronautics*, pages 111–126, 1970. A portion of this study was conducted under NASA Contract NAS 3-12025, Lewis Research Center.
- [7] G.R. Cunningham and C.L. Tien. A study of heat-transfer processes in multilayer insulations. In Jerry T. Bevens, editor, *Thermophysics: Applications to Thermal Design of Spacecraft*, pages 111–126. Academic Press, New York and London, 1970.
- [8] Lady (editor) Dewar. *Collected papers of Sir James Dewar*, volume 1 and 2. Cambridge University Press, 1927.
- [9] T. Echániz, R.B. Pérez-Sáez, and M.J. Tello. Optical properties of metals: infrared emissivity in the anomalous skin effect spectral region. *Journal of Applied Physics*, (116), 2014. 093508.
- [10] M. M. Finckenor and D. D. Dooling. Multilayer insulation material guidelines. Technical Report TP-1999-209263, NASA, Apr 1998.
- [11] David G. Gilmore, editor. *Spacecraft Thermal Control Handbook*, volume 1. The Aerospace Press, 2 edition, 2002.
- [12] DeWitt Incropera, Bergman, and Lavine. *Fundamentals of Heat and Mass Transfer*. Wiley, 6 edition, 2007.
- [13] Max Jakob, editor. *Heat transfer*, volume 1. Wiley, 1949.

- [14] Lonny Kauder. Spacecraft thermal control coatings references. Technical Report NASA/TP-2005-212792, NASA, Dec 2005.
- [15] C.W. Keller, G.R. Cunningham, and A.P. Glassford. Thermal performance of multilayer insulations. Technical Report NASA-CR-134477 & LMSC-D349866, Lockheed Missiles and Space Co., Apr 1974. Sunnyvale, Calif.
- [16] C.W. Keller, G.R. Cunningham, and A.P. Glassford. Thermal performance of multilayer insulations. Technical Report NASA CR-134477, Lockheed Missiles & Space Company, Inc., Apr 1974.
- [17] E.I. Lin, J.W. Stultz, and R.T. Reeve. Effective emittance for cassini multilayer insulation blankets and heat loss near seams. *J. of Thermophysics and Heat Transfer*, 10(2), 1996. April-June.
- [18] Glen E. McIntosh. Layer by layer mli calculation using a separated mode equation. Cryogenic Engineering Conference, 1993.
- [19] T. Ohmori, A. Yamamoto, and M. Nakajima. The effect of non-zero thermal radiation transmissivity of the aluminized mylar film on the thermal performance of super-insulation. *Advances in Cryogenic Engineering: Proceedings of the Cryogenic Engineering Conference*, pages 1573–1582, 1960.
- [20] Ron Ross. Calculation of the thermal radiation properties of low-emissivity surfaces at temperatures below 50 k. 2006. Unpublished draft available by request.
- [21] Q.S. Shu. Systematic study to reduce the effects of cracks in multilayer insulation part 1: theoretical model. *Cryogenics*, 27:249–256, May 1987. Fermi National Accelerator Laboratory.
- [22] Q.S. Shu, R.W. Fast, and H.L. Hart. Systematic study to reduce the effects of cracks in multilayer insulation part 2: experimental results. *Cryogenics*, 27:298–311, June 1987.
- [23] Robert Siegel and John R. Howell. *Thermal Radiation Heat Transfer*. Hemisphere Publishing Corporation, 3 edition, 1992.
- [24] J. Srinivasan. A paradox in radiation heat transfer. *AIP Advances*, pages 85–91, 2007. Centre for Atmospheric and Oceanic Sciences and Mechanical Engineering, Indian Institute of Science.
- [25] C.L. Tien. A correlation for thermal contact conductance of nominally flat surfaces in vacuum. pages 755–759. Proceedings of the Seventh Thermal Conductivity Conference, September 1968. NBS SP-302.
- [26] C.L. Tien and G.R. Cunningham. Cryogenic insulation heat transfer. *Advances in Heat Transfer*, 9:349–417, 1973.



Thermal Desktop Validation Case  
Two parallel plates

Consider two 1m<sup>2</sup> square parallel plates spaced 1 m apart. The backsides of the plates are adiabatic. Assume 1000W are dissipated in one plate. What is the final steady state result? Compare the analytical solution to Thermal Desktop. This is a simple constant properties, gray-diffuse, steady state solution in large, isothermal surroundings at 100K.

According to the figure in Fundamentals of Heat Transfer, two parallel plates with  $X = 1$  and  $Y = 1$  gives a view factor of 0.2.

$$\begin{aligned}
 F_{12} &:= 0.2 & F_{13} &:= 0.8 & A_1 &:= 1\text{m}^2 & T_{\text{sur}} &:= 100\text{K} & \epsilon_1 &:= 0.11 \\
 F_{21} &:= 0.2 & F_{23} &:= 0.8 & A_2 &:= 1\text{m}^2 & & & \epsilon_2 &:= 0.11
 \end{aligned}$$

$$q_1(J_1, J_2) := \frac{J_1 - J_2}{\frac{1}{A_1 F_{12}}} + \frac{J_1 - E_b(T_{\text{sur}})}{\frac{1}{A_1 F_{13}}} \quad q_2(J_1, J_2) := \frac{J_2 - J_1}{\frac{1}{A_2 F_{21}}} + \frac{J_2 - E_b(T_{\text{sur}})}{\frac{1}{A_2 F_{23}}}$$

$$J_1 := 1000 \frac{\text{W}}{\text{m}^2} \quad J_2 := 100 \frac{\text{W}}{\text{m}^2} \quad \text{radiosity initialization}$$

Given

$$q_1(J_1, J_2) = 1000\text{W}$$

$$q_2(J_1, J_2) = 0\text{W}$$

$$\begin{pmatrix} J_1 \\ J_2 \end{pmatrix} := \text{Find}(J_1, J_2)$$

given/find solve block with 'constraint equals sign' setting the heat flow from plate 1 (lower plate in Thermal Desktop) to plate 2 and the large isothermal surroundings to 1000W.

$$J_1 = 1047.34 \frac{\text{W}}{\text{m}^2} \quad J_2 = 214.00 \frac{\text{W}}{\text{m}^2}$$

$$q_{1e}(T_1) := \frac{J_1 - \sigma \cdot T_1^4}{\left( \frac{1 - \epsilon_1}{A_1 \cdot \epsilon_1} \right)} \quad T_1 := 300\text{K}$$

Given

$$q_{1e}(T_1) = -1000\text{W}$$

$$T_1 := \text{Find}(T_1) \quad T_1 = 360.46 \text{ } ^\circ\text{C} \quad \text{converted} \quad T_1 = 633.61 \text{ K} \quad T_1 = 680.82 \text{ } ^\circ\text{F}$$

**Figure 14:** A radiation network and the radiosity method is used to solve this basic heat transfer problem.

$$q_{2e}(T_2) := \frac{J_2 - \sigma \cdot T_2^4}{\left( \frac{1 - \epsilon_2}{A_2 \cdot \epsilon_2} \right)}$$

$T_2 := 250\text{K}$  Given

$$q_{2e}(T_2) = 0\text{W}$$

$$T_{2,\text{new}} := \text{Find}(T_2)$$

$T_2 = -25.29^\circ\text{C}$  converted  $T_2 = 247.86\text{K}$   $T_2 = -13.52^\circ\text{F}$

Here, I found that the plate temperatures to be 633.61 K and 247 K. I had to be careful to account for the source heat flow through the heated surface. Below, I show a TD plot of the equivalent finite difference model. The TD model gave 248.9 K and 633.6 K, which is almost exactly the same answer.

When I went ahead and changed the monte Carlo ray tracing to 50,000 rays from 5000, the temperatures changed to 247.4 K and 633.7 K.

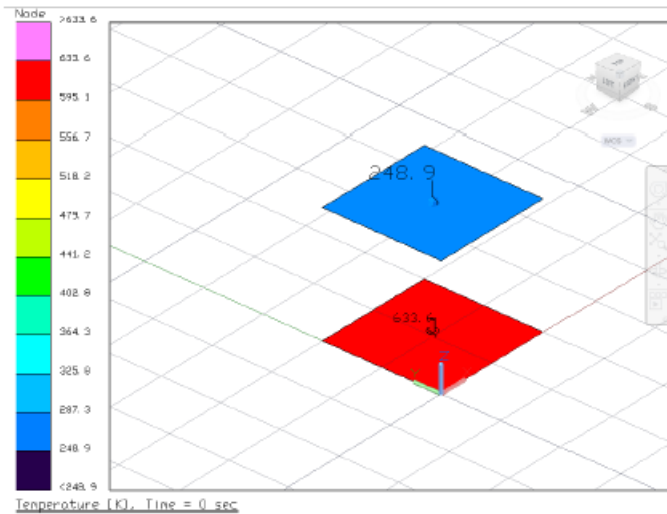


**Figure 15:** This figure shows the result of the solution from this problem, as well as the associated Thermal Desktop results.

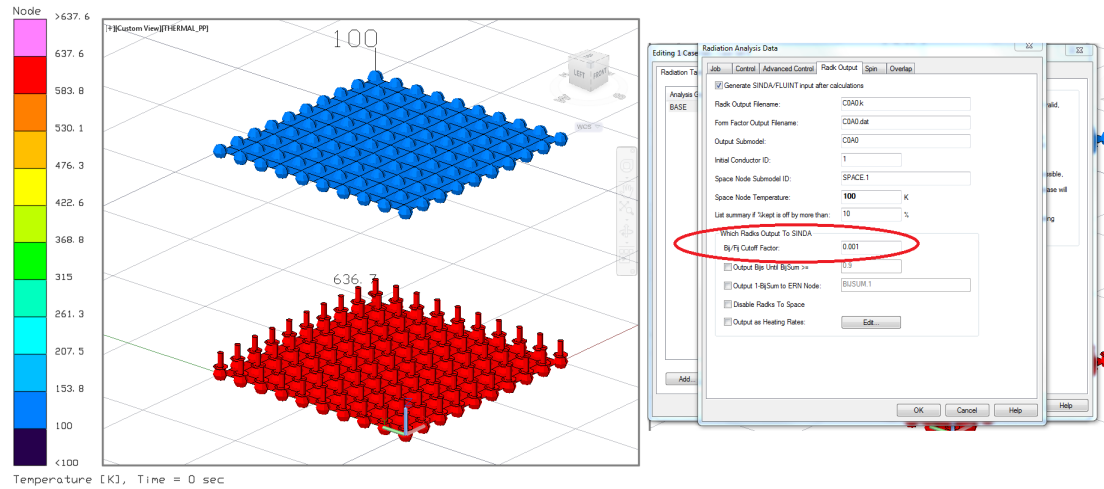


**Figure 16:** In this case, the Bij cutoff factor was set too low for the number of nodes and rays being shot, therefore, many of the rays (having failed the Bij/Fij) were neglected from the resultant, leading to a lower predicted temperature.

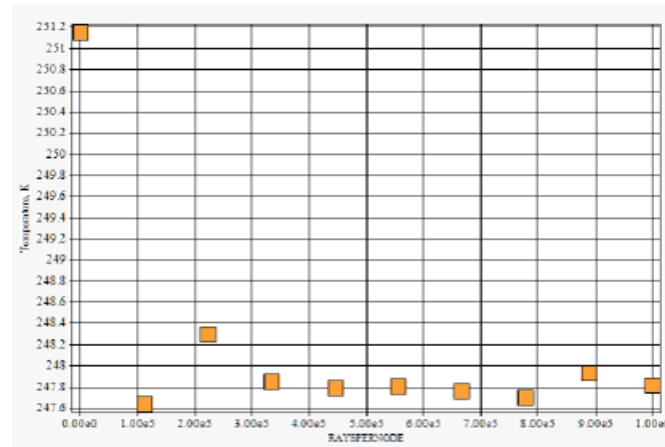


**Figure 17:** Variation in the plate node average temperature settles, in this case, once 300,000 rays per node are shot (1 x 1 plate mesh case). There is an interesting jump near 100,000 rays per node that is hard to explain.

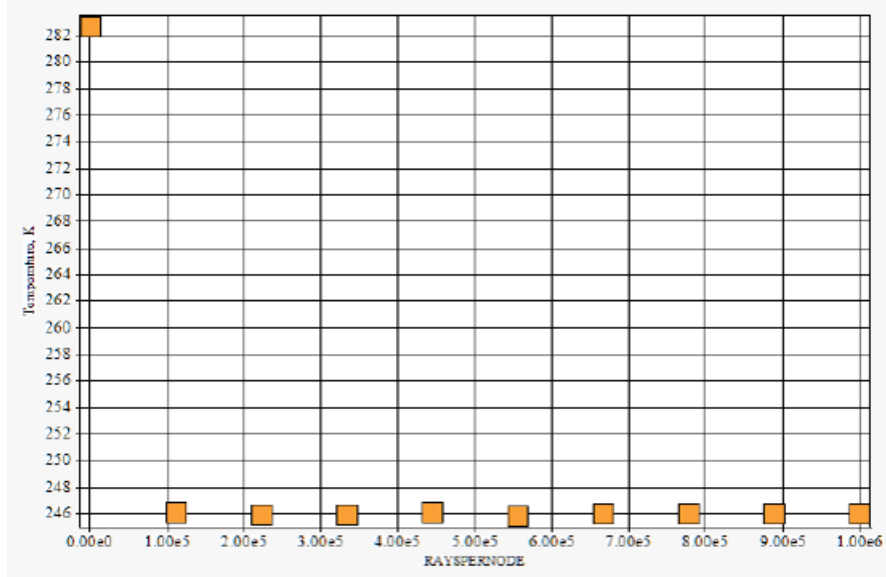


**Figure 18:** Variation in the plate node average temperature settles, in this case, once 100,000 rays per node are shot (10 x 10 plate mesh case).

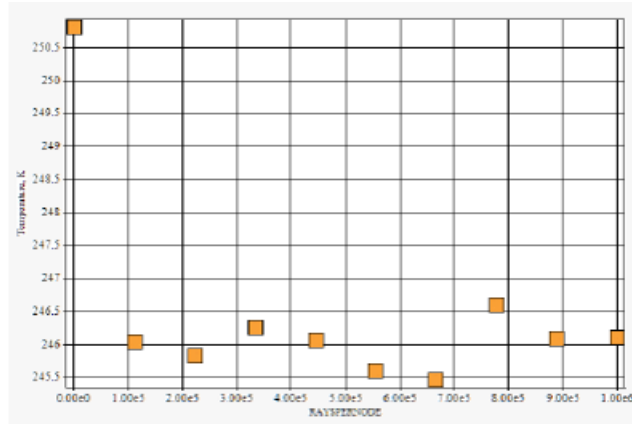


**Figure 19:** Variation in the plate node average temperature settles, in this case, once 100,000 rays per node are shot (10 x 10 plate mesh case using the progressive radiosity method, as opposed to the Monte Carlo method used in all other cases).

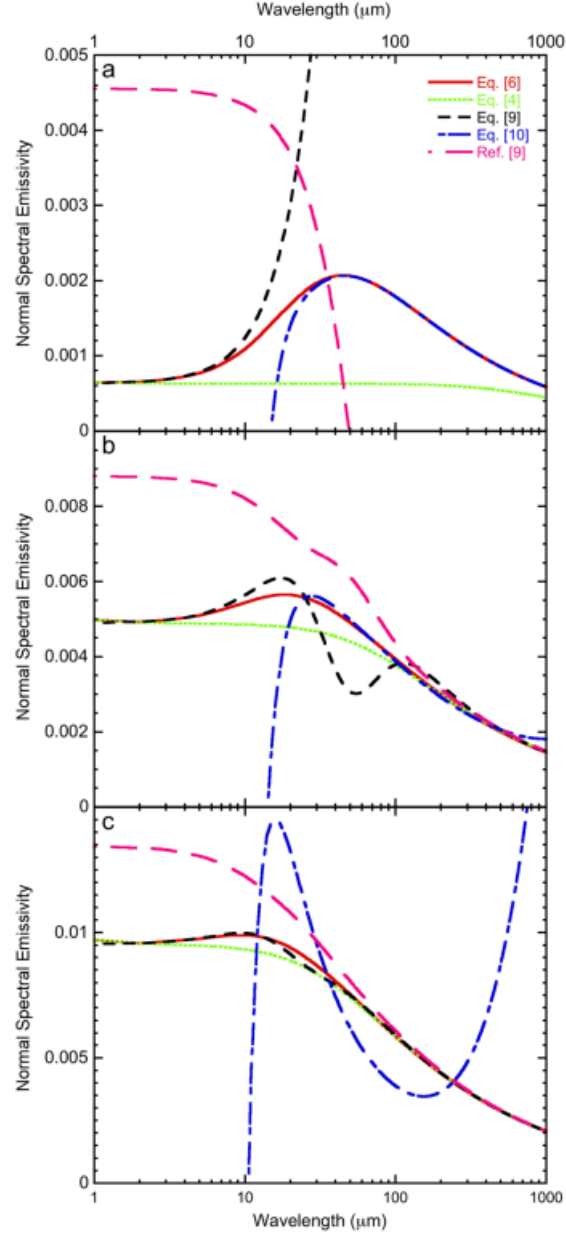
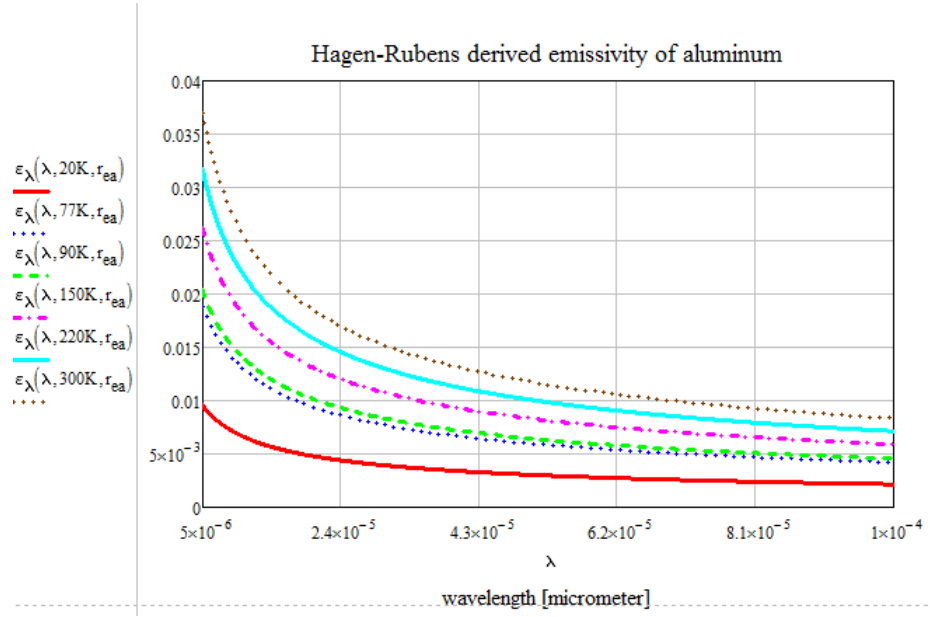


FIG. 1. Classical and anomalous skin effect emissivities given by Eq. (4) (dotted, green), Eq. (6) (solid, red), Eq. (9) (dashed, black), Eq. (10) (dotted-dashed, blue) and series expansion for  $p=0$  (long-dashed, pink).<sup>9</sup> (a)  $T = 80$  K, (b)  $T = 293$  K, and (c)  $T = 526$  K. The physical parameters used are those for copper in Table I.

**Figure 20:** Figure by T. Echániz et al. [9].

$$\begin{aligned}
\epsilon_{\lambda n}(\lambda, t, r_{e273}) &:= 36.5 \cdot \left( \frac{\mu\text{m}}{\Omega \cdot \text{cm}} \right)^2 \cdot \left( \frac{r_{e273}}{273\text{K}} \cdot t \right)^{\frac{1}{2}} - 464 \cdot \left( \frac{\mu\text{m}}{\Omega \cdot \text{cm}} \right) \frac{r_{e273}}{\lambda} \\
C_1 &:= 3.742 \cdot 10^8 \frac{\text{W} \cdot (\mu\text{m})^4}{\text{m}^2} \quad C_2 := 1.439 \cdot 10^4 \mu\text{m} \cdot \text{K} \\
e_b(\lambda, T_o) &:= \frac{C_1}{\lambda^5 \cdot \left( e^{\frac{C_2}{\lambda \cdot T_o}} - 1 \right)} \\
\epsilon_{\lambda h}(\lambda, t, r_{e273}) &:= 1.3 \cdot \epsilon_{\lambda n}(\lambda, t, r_{e273}) \\
\epsilon_{\lambda ha}(\lambda, t) &:= \epsilon_{\lambda h}(\lambda, t, 2.82 \cdot 10^{-6} \Omega \cdot \text{cm}) \\
q_a(T_1, T_2) &:= \int_5^{10000} \frac{(e_b(\lambda \cdot \mu\text{m}, T_1) - e_b(\lambda \cdot \mu\text{m}, T_2))}{\frac{1}{\epsilon_{\lambda ha}(\lambda \cdot \mu\text{m}, T_1)} + \frac{1}{\epsilon_{\lambda ha}(\lambda \cdot \mu\text{m}, T_2)} - 1} d\lambda \cdot \mu\text{m} \\
q_a(300\text{K}, 90\text{K}) &= 3.616 \cdot \frac{\text{W}}{\text{m}} \\
q_{\text{ratio}} &:= \frac{q_a(300\text{K}, 77\text{K})}{q_a(300\text{K}, 20\text{K})} = 1.637
\end{aligned}$$

**Figure 21:** Solution to the nongray dewar problem following the approach of Srinivasan [24] which keeps a two term approximation of the Hagen-Rubens relation.



**Figure 22:** Predicted temperature dependent spectral emissivities as calculated with the two term Hagen-Rubens approximation.

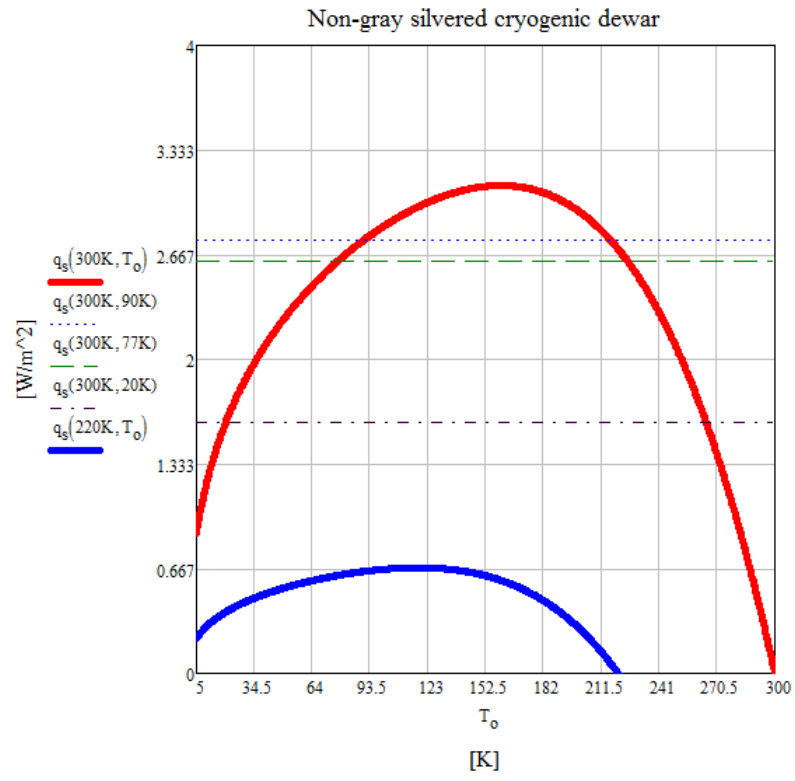


**Figure 23:** Solution to Srinivasan's problem for a dewar with both surfaces coated with silver.



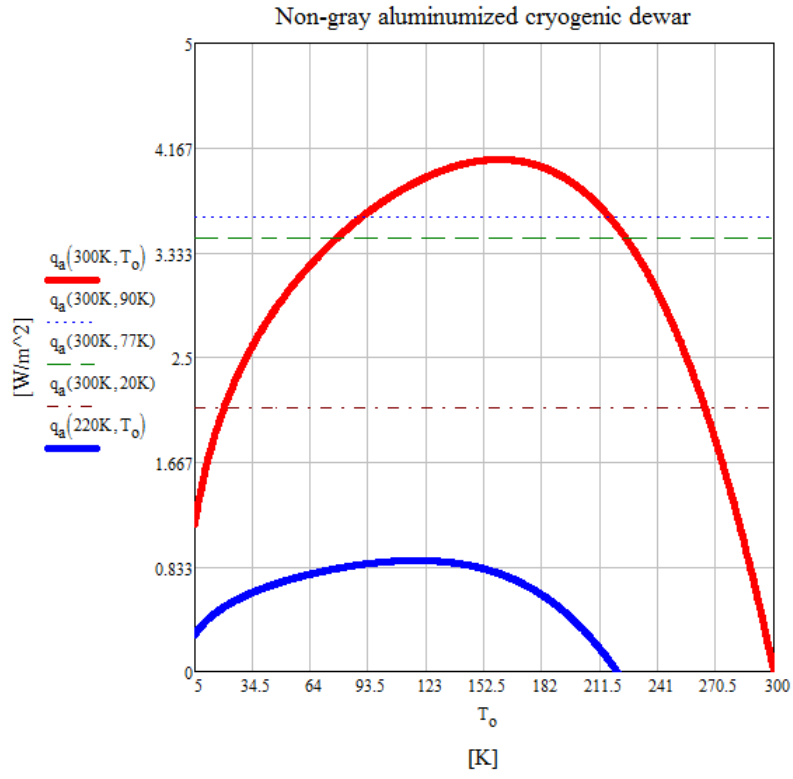


**Figure 24:** Solution to Srinivasan's problem for a dewar with both surfaces coated with aluminum.

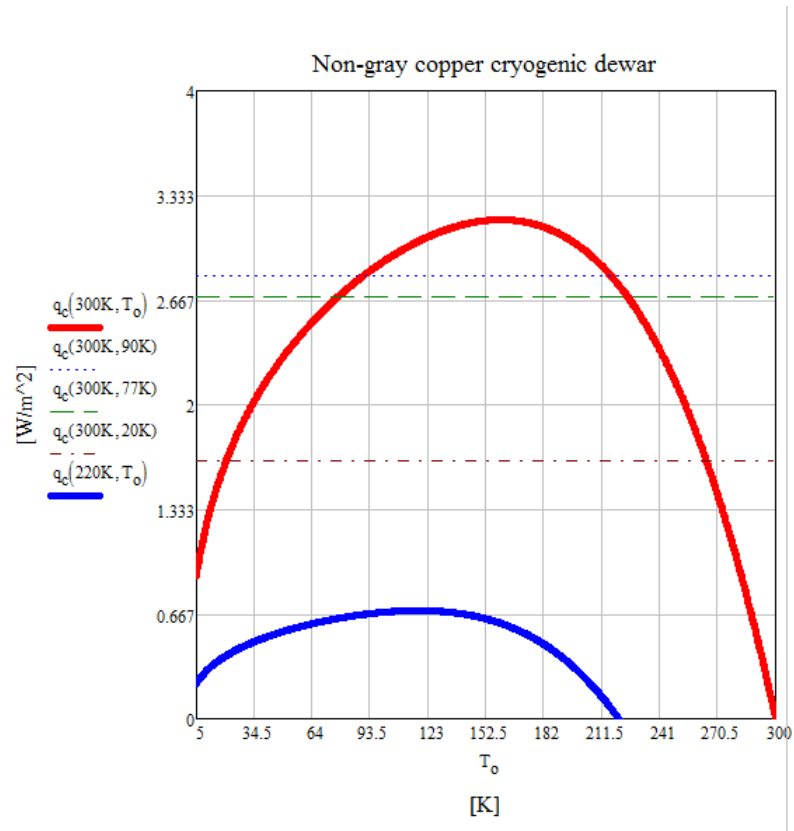


**Figure 25:** Solution to Srinivasan's problem for a dewar with both surfaces coated with copper.

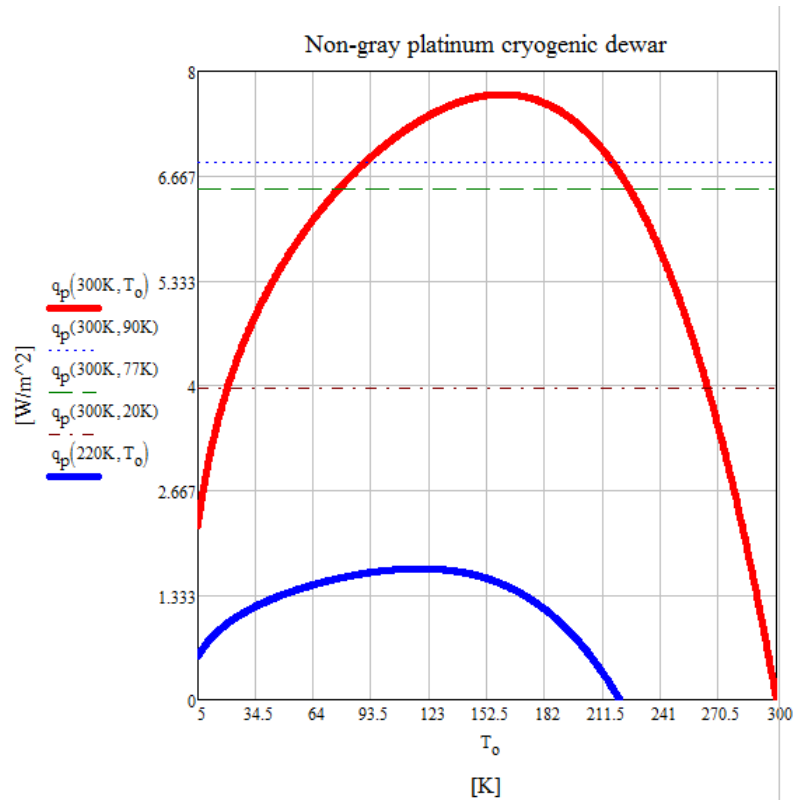


**Figure 26:** Solution to Srinivasan's problem for a dewar with both surfaces coated with platinum.

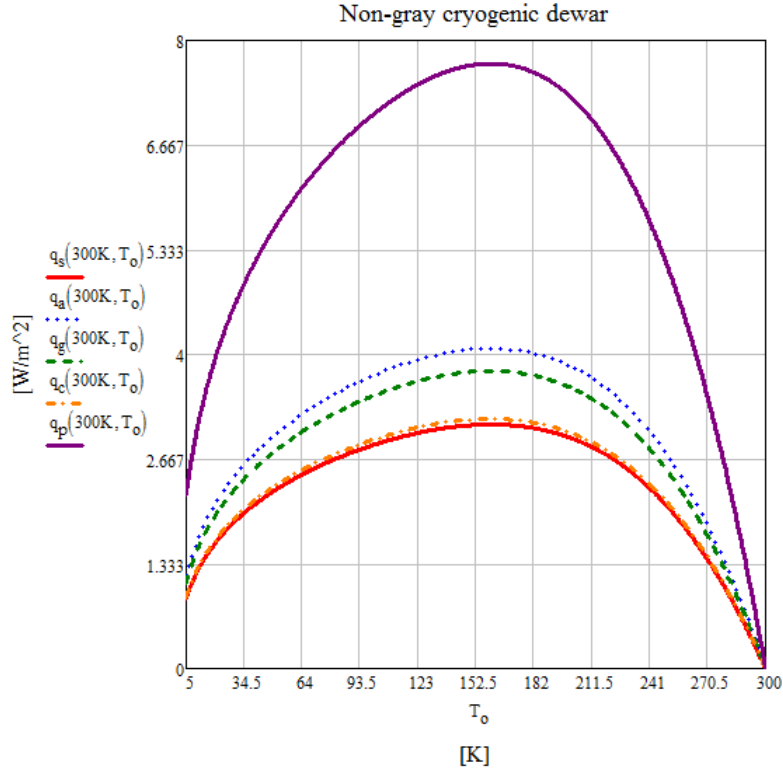


**Figure 27:** The comparison shows that platinum performs relatively poorly compared to silver and copper. Gold and aluminum seem to perform slightly worse according to the two term Hagen-Rubens non-gray approximation.

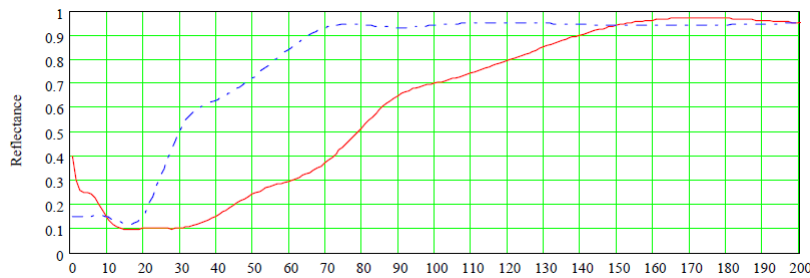


**Figure 28:** Kauder gave spectral plots for the two hypothetical coatings used in his example, note that the units are micrometer on the x-axis. Note that when trying to match these results in Thermal Desktop, it was necessary to assume this chart shows the spectral emissivity as opposed to the spectral reflectance. It seems the figure was mislabeled.

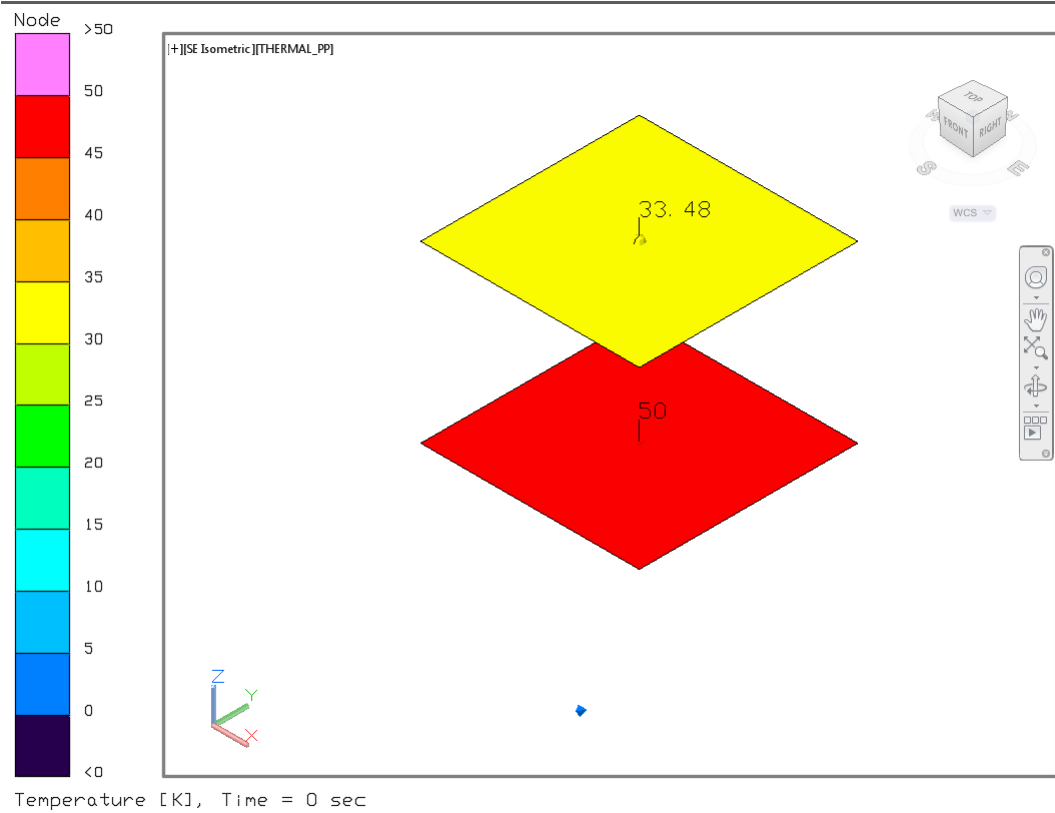


**Figure 29:** The solution to Kauder's example as performed using Thermal Desktop. Kauder reveals the analytical solution to two finite non-gray square plates in his analysis[14].

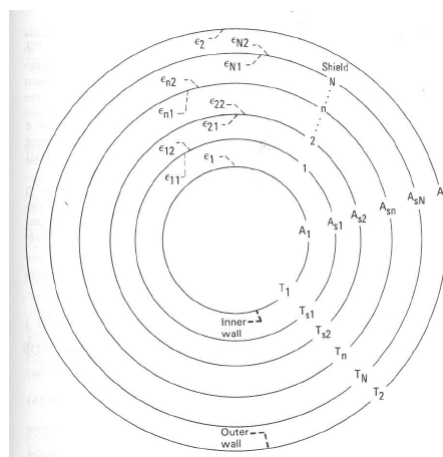


**Figure 30:** Radiation shields between concentric cylinders or spheres [23].

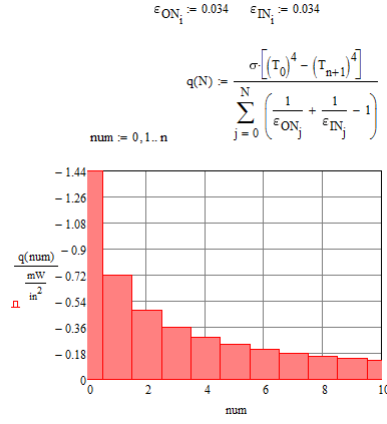
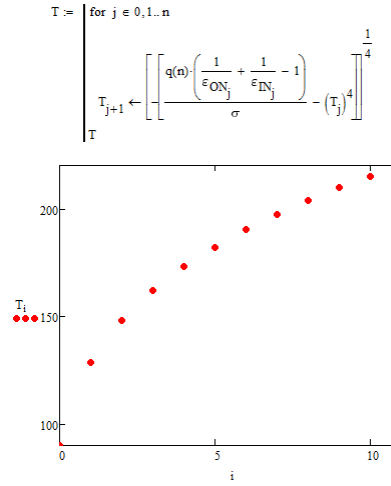


**Figure 31:** The basic ideal shields solution. The histogram shows how much the total heat leak is reduced by adding additional layers.



	0
0	90
1	128.494232696795
2	147.985784601138
3	161.873357501932
4	172.895940308192
5	182.140331040846
6	190.159179034974
7	197.27539611224
8	203.695484094032
9	209.560198194264
10	214.970157935369
11	220

**Figure 32:** The solved temperature profile for the ideal, floating shields case with ten layers.

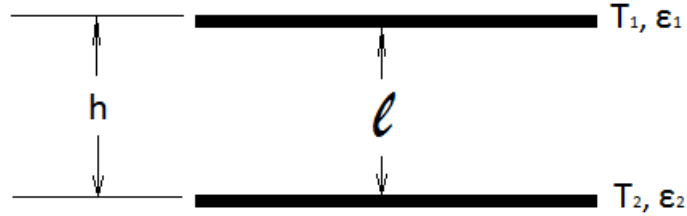


**Figure 33:** Schematic showing the starting point of the Cunnington and Tien analysis—simply two layers of insulation and their properties. Note that the temperature is assumed to exist but isn't known or prescribed.

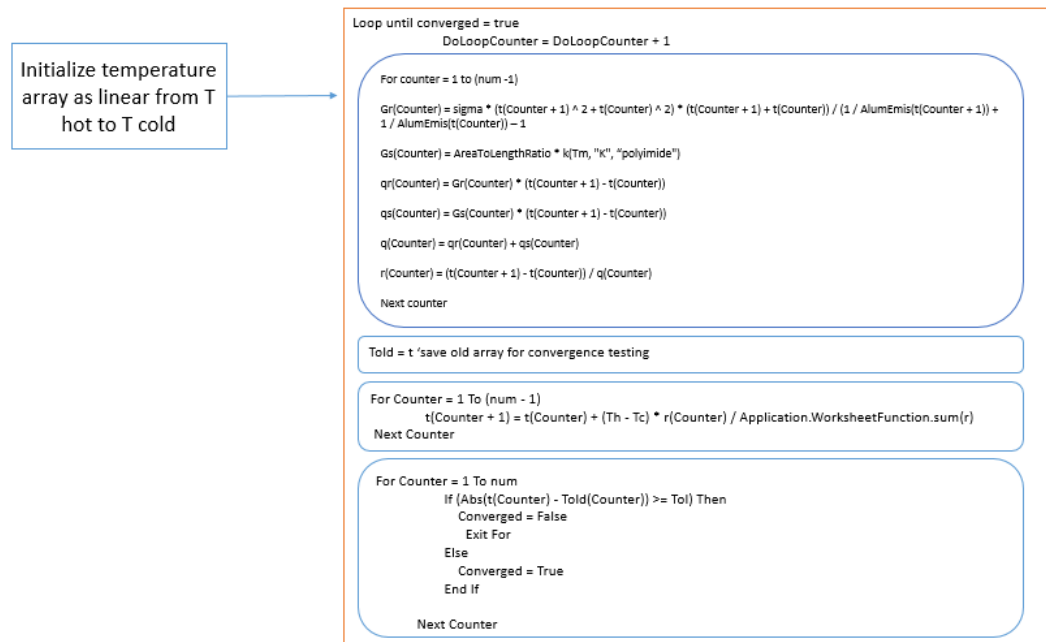


**Figure 34:** A block diagram for an iterative separated mode superinsulation model.

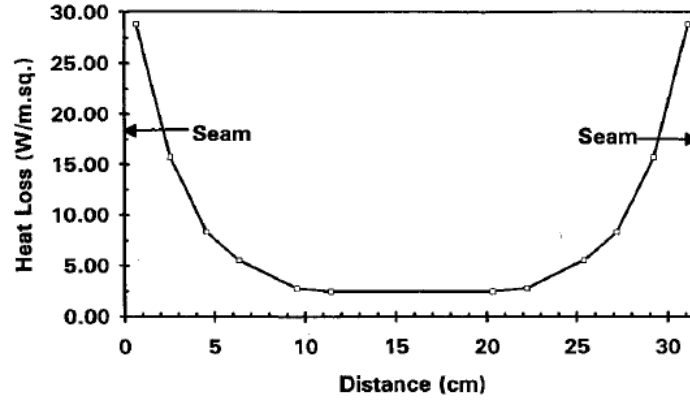


**Fig. 8 MLI-A heat loss distribution.**

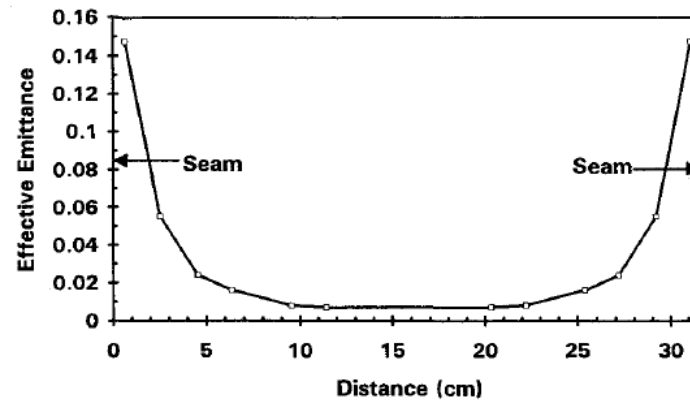


**Fig. 9 MLI-A local effective emittance.**

Figure 35: Results of the Cassini program study on multilayer blanket performance[17].

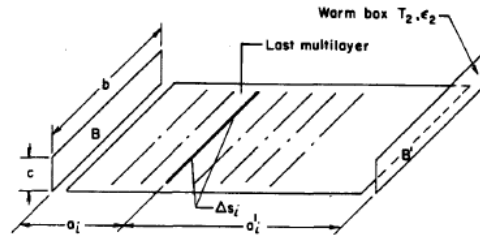


**Figure 8 Slots in a MLI blanket face the two end plans B and B' of the warm box**

Figure 36: Schematic of the geometry Shu analyzed in his 1987 study[21].



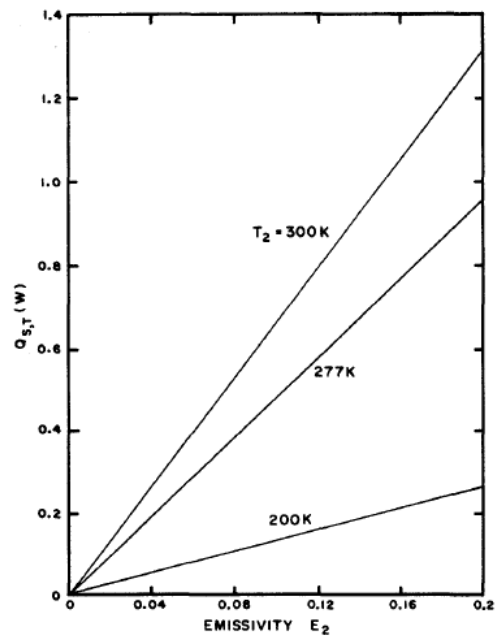


**Figure 10** Calculated total increment of heat load due to cracks,  $Q_{S,T}$ , by the enhanced black cavity model for an experimental apparatus<sup>4</sup> as a function of the emissivity,  $\epsilon_2$ , and the temperature,  $T_2$ , of the warm box. The area of seven cracks is 0.014 m<sup>2</sup>; the total area of the 30 layer MLI blanket is 2.26 m<sup>2</sup>

**Figure 37:** Results from Shu's 1987 study[21].

	case 0	case 1	case 2	case 3
	5000 rays per node	10000 rays per node	100000 rays per node	1000000 rays per node
	200 rays before initial error check	400 rays before initial error check	4000 rays before initial error check	40000 rays before initial error check
	Bij/Fij cutoff factor 0.001	Bij/Fij cutoff factor 0.001	Bij/Fij cutoff factor 0.001	Bij/Fij cutoff factor 0.001
cold sphere, blackbody	90.0000	90.0000	90.0000	90.0000
L1	122.4408	122.4808	122.4404	122.4519
L2	145.3205	145.3361	145.3335	145.3343
L3	160.6832	160.6790	160.6851	160.6838
L4	172.5579	172.5402	172.5445	172.5452
L5	182.3310	182.3328	182.3378	182.3361
L6	190.7331	190.7369	190.7327	190.7356
L7	198.1288	198.1280	198.1283	198.1280
L8	204.7569	204.7496	204.7523	204.7526
L9	210.7724	210.7742	210.7693	210.7703
L10	216.2885	216.2913	216.2930	216.2934
large, isothermal	220.0000	220.0000	220.0000	220.0000
Heat to cold node [W]	-22.07	-22.06	-22.06	-22.06
	case 4	case 5	case 6	case 7
	5000 rays per node	10000 rays per node	100000 rays per node	1000000 rays per node
	200 rays before initial error check	400 rays before initial error check	4000 rays before initial error check	40000 rays before initial error check
	Bij/Fij cutoff factor 0	Bij/Fij cutoff factor 0	Bij/Fij cutoff factor 0	Bij/Fij cutoff factor 0
	90.0000	90.0000	90.0000	90.0000
	122.5735	122.4721	122.5073	122.5073
	145.3727	145.3585	145.3597	145.3597
	160.7024	160.7017	160.6990	160.6969
	172.5515	172.5507	172.5523	172.5515
	182.3390	182.3324	182.3369	182.3375
	190.7322	190.7379	190.7326	190.7337
	198.1259	198.1239	198.1232	198.1232
	204.7409	204.7467	204.7453	204.7458
	210.7667	210.7589	210.7626	210.7616
	216.2787	216.2848	216.2823	216.2831
	220.0000	220.0000	220.0000	220.0000
	-22.13	-22.13	-22.12	-22.12

**Figure 38:** It seems a minimum of 100,000 rays with a cutoff factor of zero is acceptable for this particular geometry (case six).

Analytical solution	Thermal Desktop solution
90	90.0000
128.494	128.9190
147.986	148.4690
161.873	162.3760
172.896	173.4180
182.14	182.6130
190.159	190.5390
197.275	197.5990
203.695	203.9480
209.56	209.7310
214.97	215.0610
220	220.0000

**Figure 39:** The Thermal Desktop solution for this test case of floating shields has satisfactory agreement.

Max	152.6816	L1.73
Min	129.9445	L1.18
Avg	132.6128	
Max	170.2659	L2.21
Min	149.7758	L2.102
Avg	152.3661	
Max	179.9728	L3.115
Min	163.807	L3.15
Avg	165.9835	
Max	186.6893	L4.105
Min	174.8673	L4.15
Avg	176.5706	
Max	192.0007	L5.21
Min	184.0963	L5.67
Avg	185.3337	
Max	196.562	L6.105
Min	192.0684	L6.68
Avg	192.8743	
Max	200.9271	L7.62
Min	199.102	L7.15
Avg	199.546	
Max	206.33	L8.20
Min	204.5007	L8.41
Avg	205.577	
Max	211.6336	L9.61
Min	209.0299	L9.83
Avg	211.1354	
Max	216.6273	L10.61
Min	214.6969	L10.83
Avg	216.3677	

**Figure 40:** Temperature profile with maximum and minimum temperature nodes being shown for case 1.

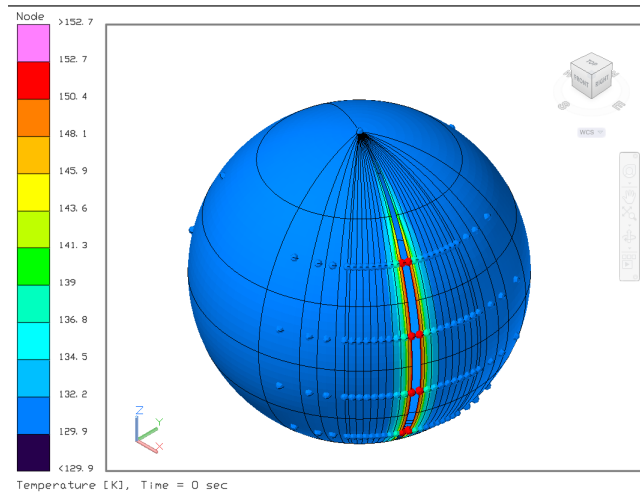


**Figure 41:** Case 1, layer 1.

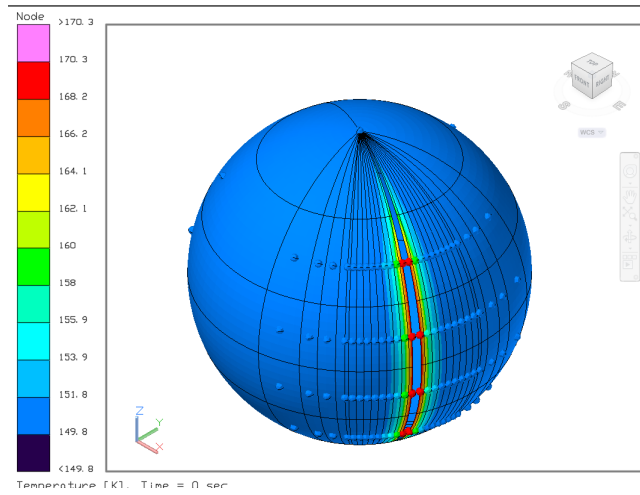


**Figure 42:** Case 1, layer 2.

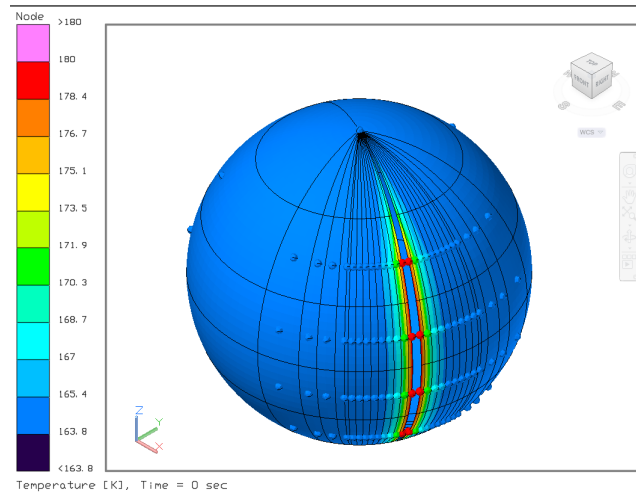


**Figure 43:** Case 1, layer 3.

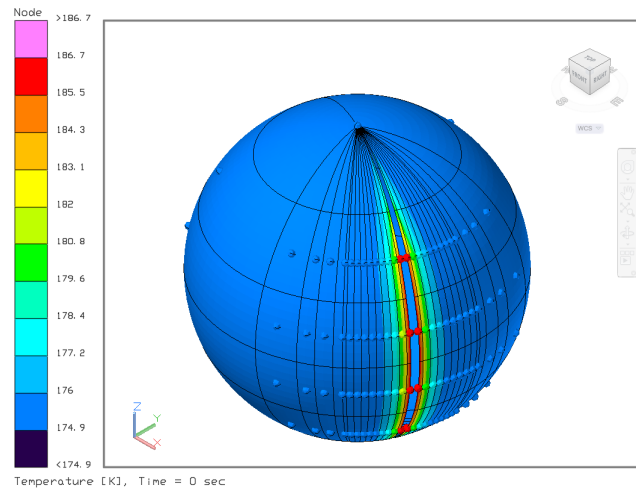


**Figure 44:** Case 1, layer 4.

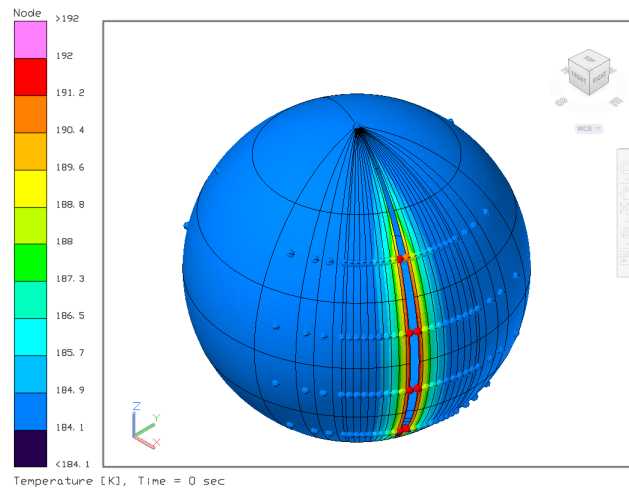


**Figure 45:** Case 1, layer 5.

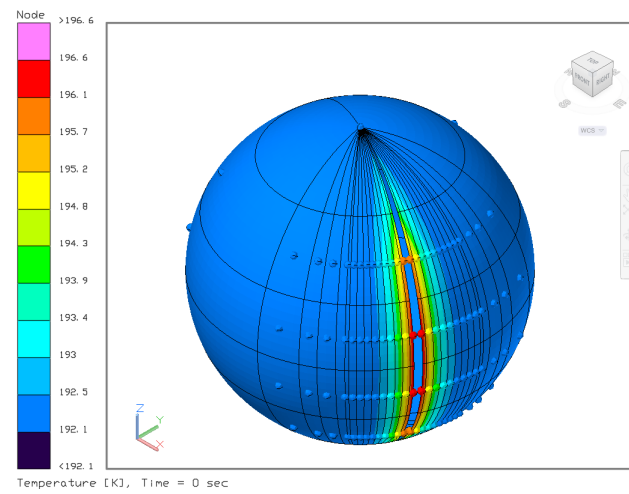


**Figure 46:** Case 1, layer 6.

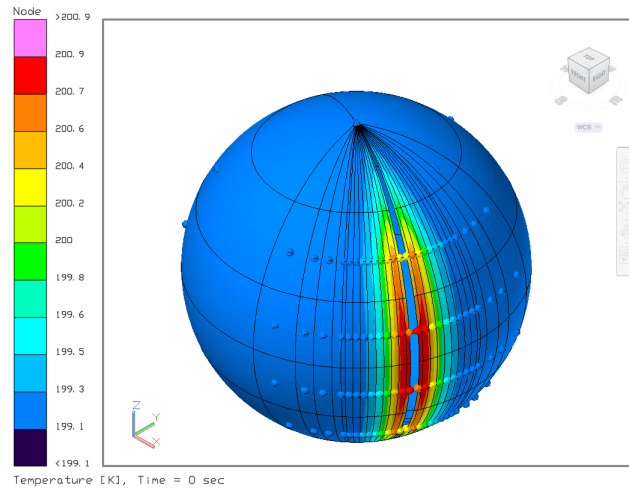


**Figure 47:** Case 1, layer 7.

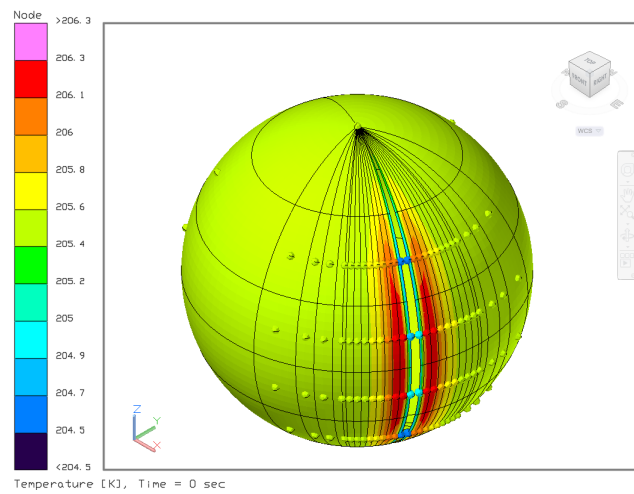


**Figure 48:** Case 1, layer 8.

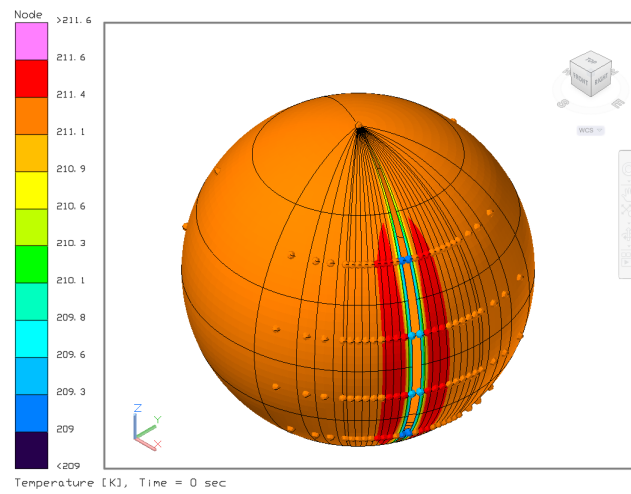


**Figure 49:** Case 1, layer 9.

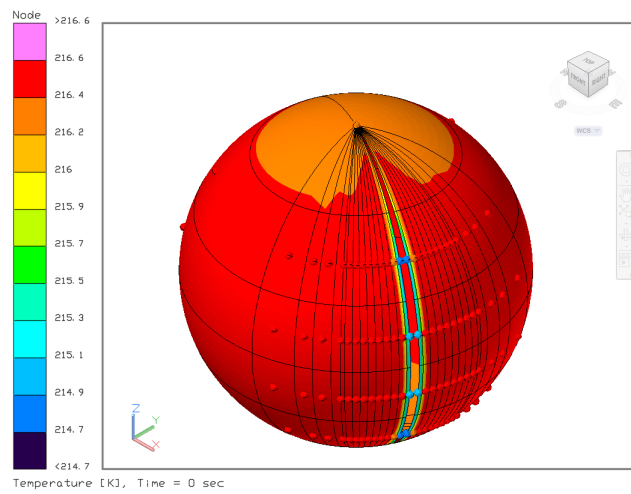


**Figure 50:** Case 1, layer 10.



Max	152.6816	L1.73
Min	129.9445	L1.18
Avg	132.6128	
Max	170.2659	L2.21
Min	149.7758	L2.102
Avg	152.3661	
Max	179.9728	L3.115
Min	163.807	L3.15
Avg	165.9835	
Max	186.6893	L4.105
Min	174.8673	L4.15
Avg	176.5706	
Max	192.0007	L5.21
Min	184.0963	L5.67
Avg	185.3337	
Max	196.562	L6.105
Min	192.0684	L6.68
Avg	192.8743	
Max	200.9271	L7.62
Min	199.102	L7.15
Avg	199.546	
Max	206.33	L8.20
Min	204.5007	L8.41
Avg	205.577	
Max	211.6336	L9.61
Min	209.0299	L9.83
Avg	211.1354	
Max	216.6273	L10.61
Min	214.6969	L10.83
Avg	216.3677	

**Figure 51:** Temperature profile with maximum and minimum temperature nodes being shown for case 4.

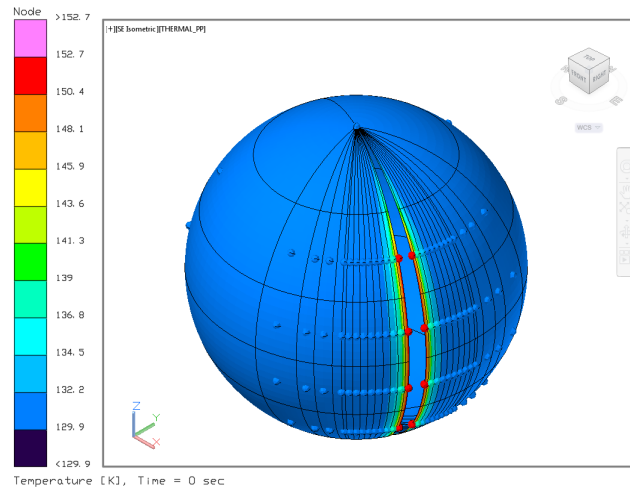


**Figure 52:** Case 4, layer 1.

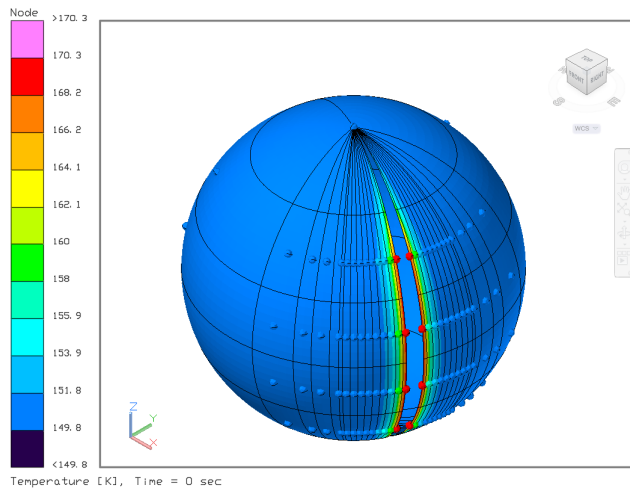


**Figure 53:** Case 4, layer 2.

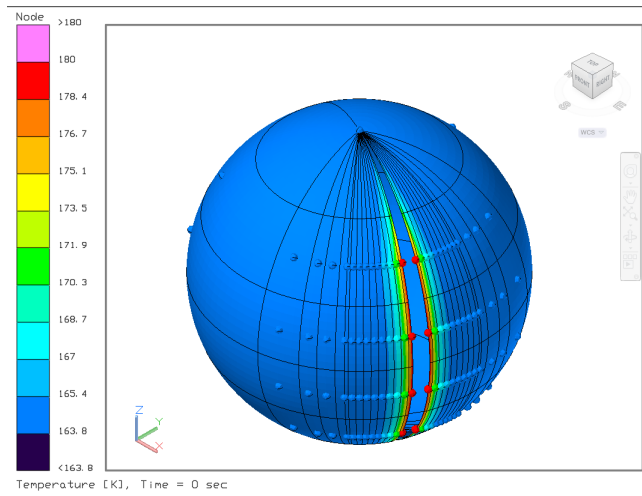


**Figure 54:** Case 4, layer 3.

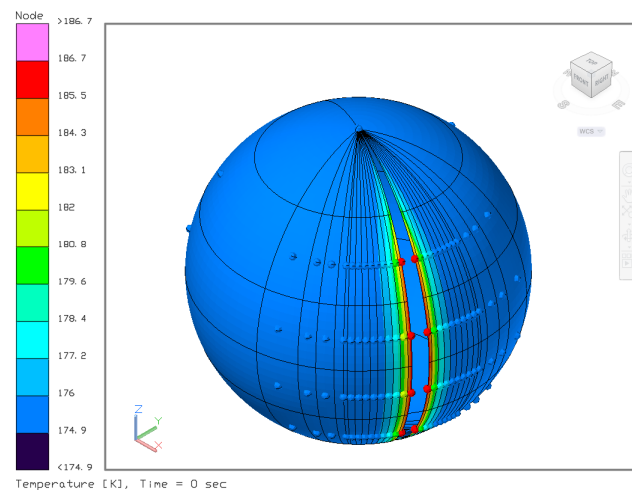


**Figure 55:** Case 4, layer 4.

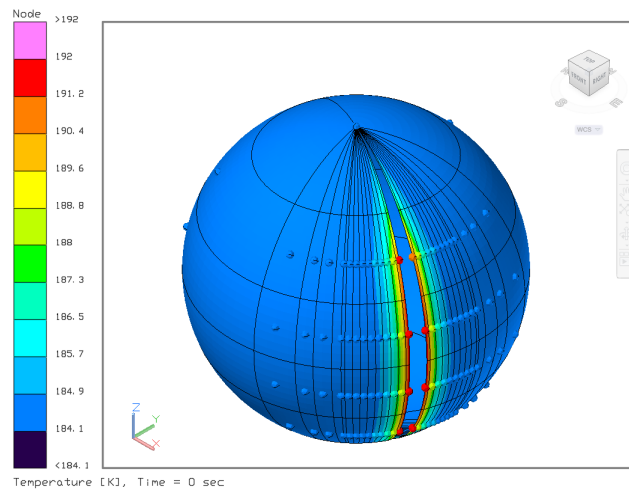


**Figure 56:** Case 4, layer 5.

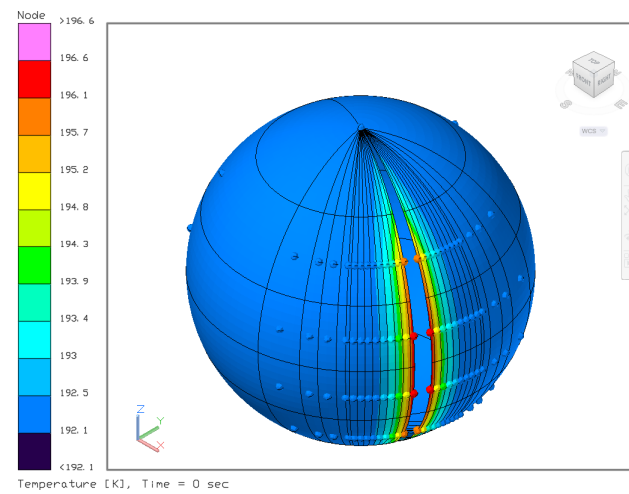


**Figure 57:** Case 4, layer 6.

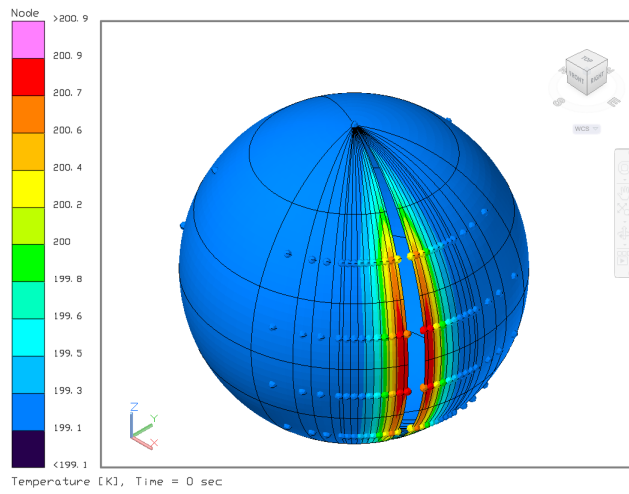


**Figure 58:** Case 4, layer 7.

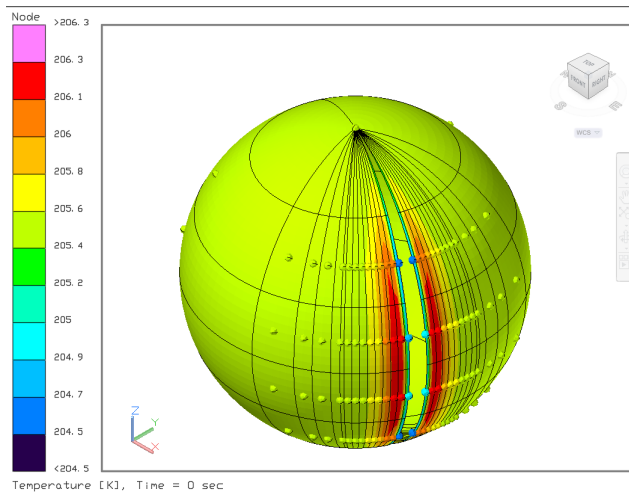


**Figure 59:** Case 4, layer 8.

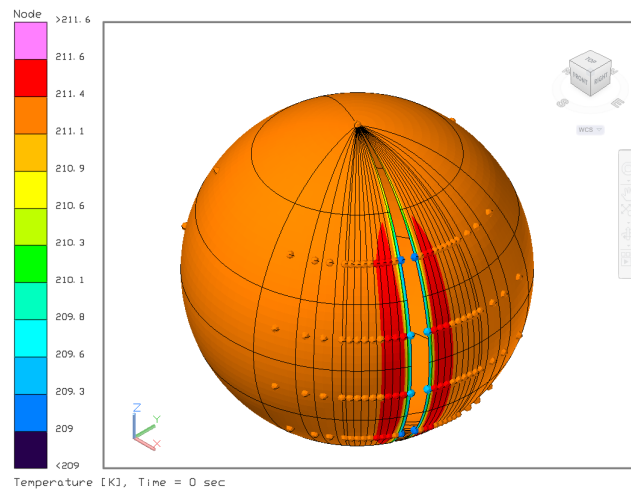


**Figure 60:** Case 4, layer 9.

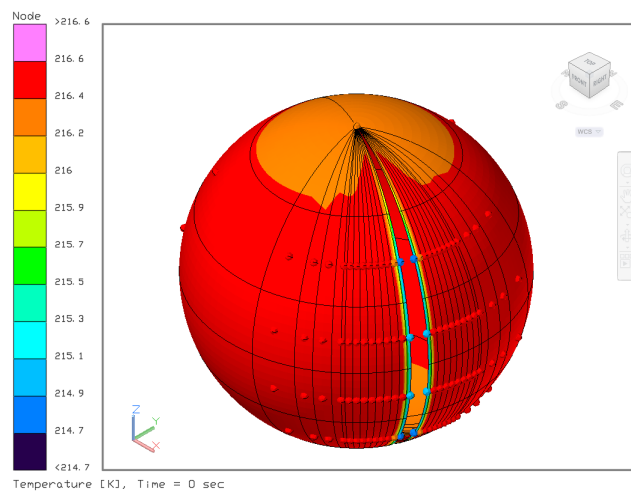


**Figure 61:** Case 4, layer 10.

Max	161.8378	L1.116
Min	129.9635	L1.28
Avg	134.4357	
Max	178.2733	L2.44
Min	149.7964	L2.99
Avg	154.3014	
Max	186.8188	L3.54
Min	163.8181	L3.28
Avg	167.7923	
Max	192.443	L4.64
Min	174.8829	L4.26
Avg	178.1517	
Max	196.608	L5.96
Min	184.1107	L5.69
Avg	186.6412	
Max	200.0353	L6.22
Min	192.0735	L6.58
Avg	193.8957	
Max	203.4101	L7.97
Min	199.1112	L7.16
Avg	200.2861	
Max	207.8292	L8.55
Min	205.4248	L8.110
Avg	206.0566	
Max	212.4319	L9.108
Min	209.0719	L9.116
Avg	211.389	
Max	216.9195	L10.98
Min	214.2788	L10.116
Avg	216.4475	

**Figure 62:** Temperature profile with maximum and minimum temperature nodes being shown for case 5.

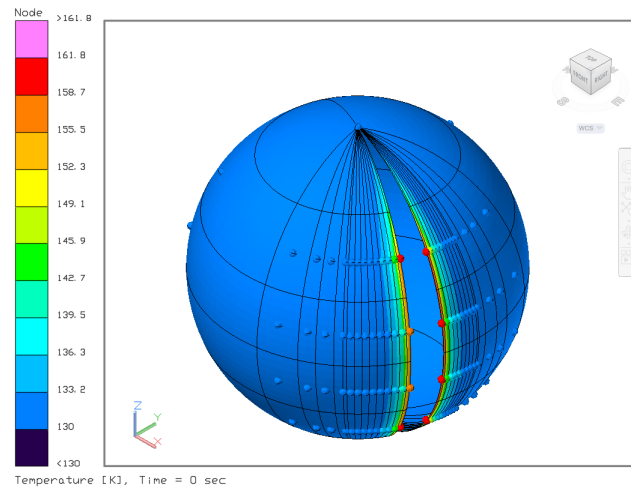


**Figure 63:** Case 5, layer 1.

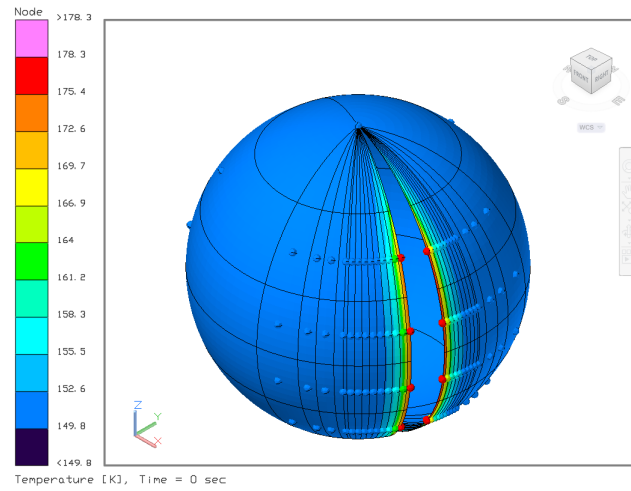


**Figure 64:** Case 5, layer 2.



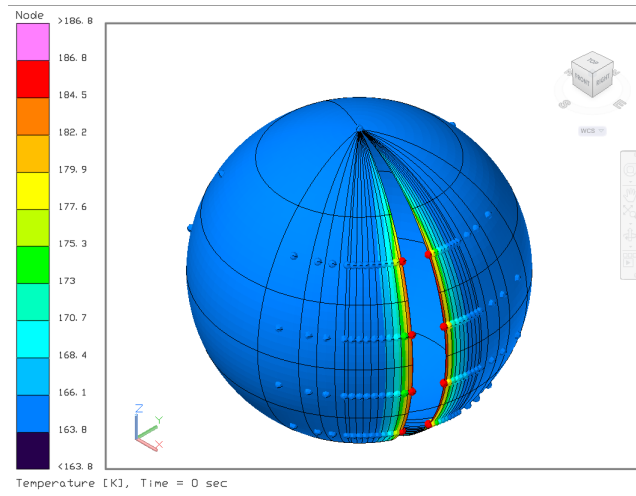


**Figure 65:** Case 5, layer 3.

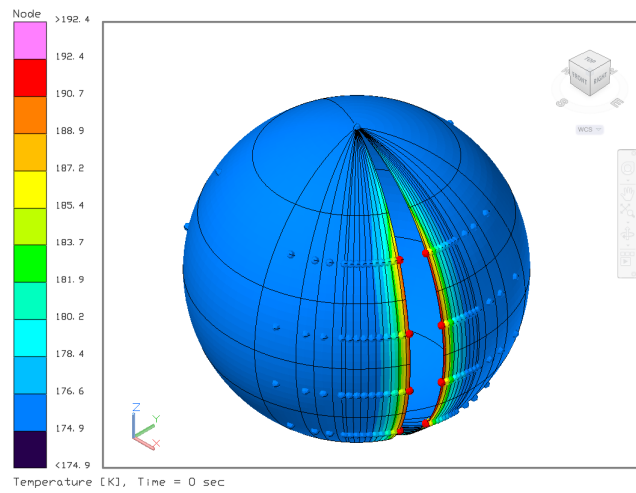


**Figure 66:** Case 5, layer 4.

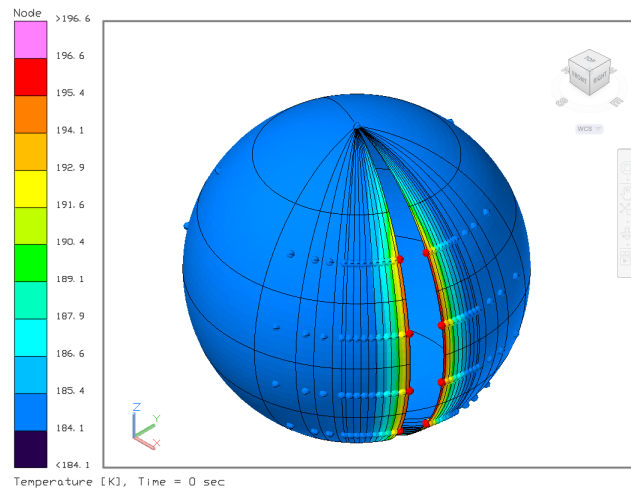


**Figure 67:** Case 5, layer 5.

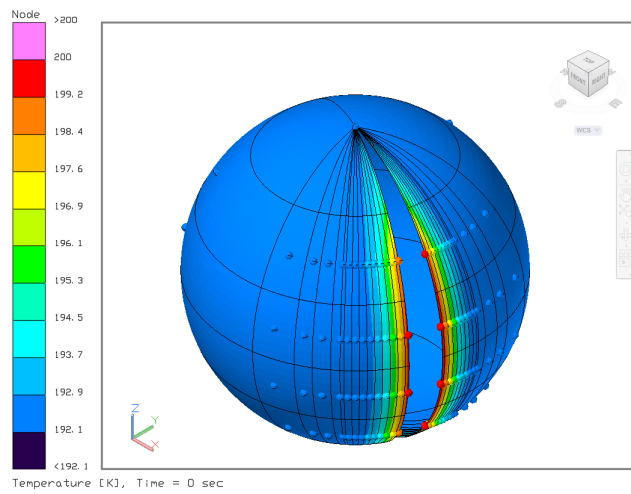


**Figure 68:** Case 5, layer 6.

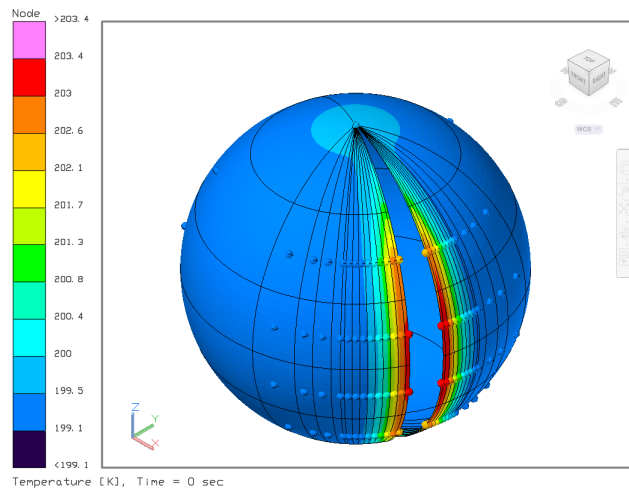


**Figure 69:** Case 5, layer 7.

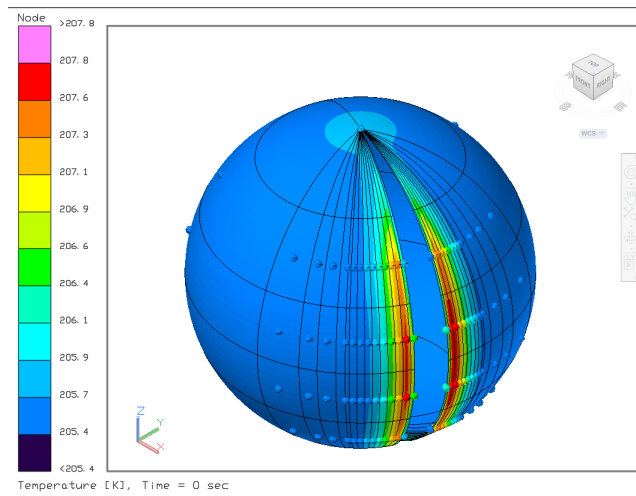


**Figure 70:** Case 5, layer 8.

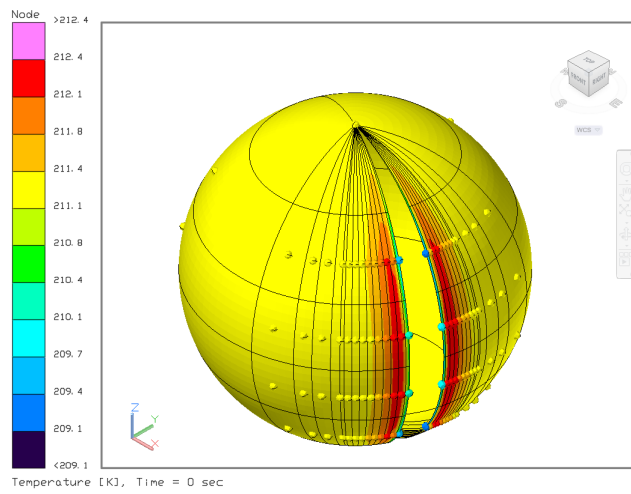


**Figure 71:** Case 5, layer 9.

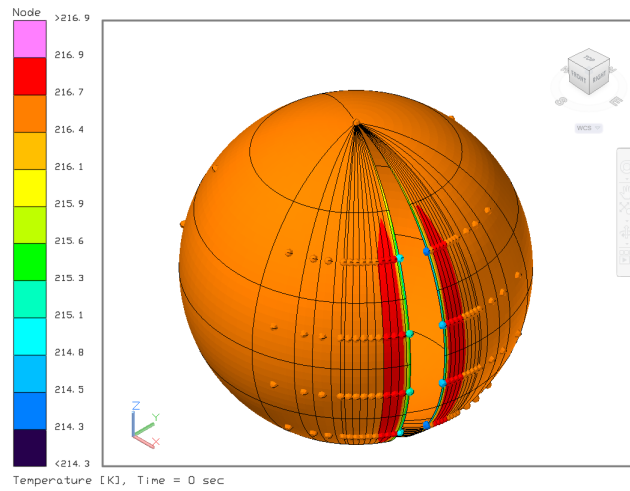


**Figure 72:** Case 5, layer 10.

Max	147.1195	L1.83
Min	129.2035	L1.19
Avg	131.1868	
Max	163.6425	L2.41
Min	148.945	L2.97
Avg	150.6209	
Max	173.0287	L3.105
Min	162.8455	L3.13
Avg	164.0852	
Max	179.739	L4.105
Min	173.8355	L4.15
Avg	174.6013	
Max	185.1514	L5.21
Min	183.0052	L5.59
Avg	183.3381	
Max	191.1281	L6.102
Min	189.6269	L6.95
Avg	190.8858	
Max	197.9967	L7.79
Min	194.1399	L7.53
Avg	197.5959	
Max	204.2361	L8.15
Min	198.6933	L8.41
Avg	203.699	
Max	209.9405	L9.9
Min	203.845	L9.83
Avg	209.367	
Max	215.1785	L10.21
Min	210.3867	L10.53
Avg	214.7492	

**Figure 73:** Temperature profile with maximum and minimum temperature nodes being shown for case 6.

Max	147.8419	L1.83
Min	124.3981	L1.4
Avg	127.1746	
Max	167.0055	L2.21
Min	144.8887	L2.101
Avg	147.6863	
Max	177.6589	L3.105
Min	159.7666	L3.17
Avg	162.1725	
Max	184.944	L4.115
Min	171.5951	L4.29
Avg	173.4964	
Max	190.6747	L5.21
Min	181.4603	L5.70
Avg	182.8808	
Max	195.4913	L6.105
Min	189.9819	L6.68
Avg	190.9511	
Max	199.9051	L7.96
Min	197.515	L7.6
Avg	198.0807	
Max	205.4674	L8.20
Min	203.7972	L8.11
Avg	204.512	
Max	210.9767	L9.61
Min	208.5637	L9.83
Avg	210.4256	
Max	216.2649	L10.71
Min	214.3629	L10.116
Avg	215.9742	

**Figure 74:** Temperature profile with maximum and minimum temperature nodes being shown for case 7.

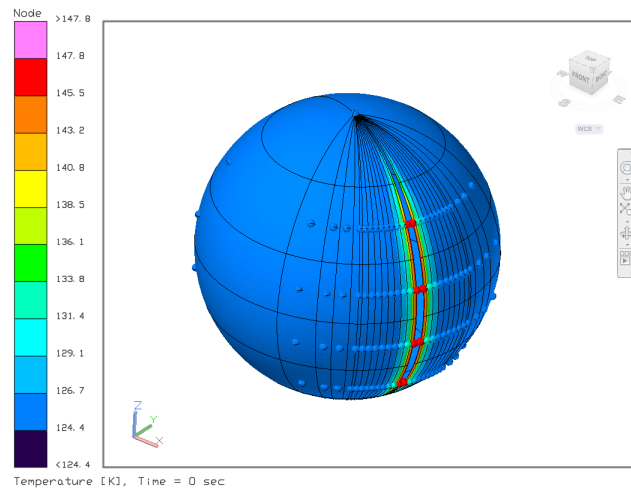


**Figure 75:** Case 7, layer 1.

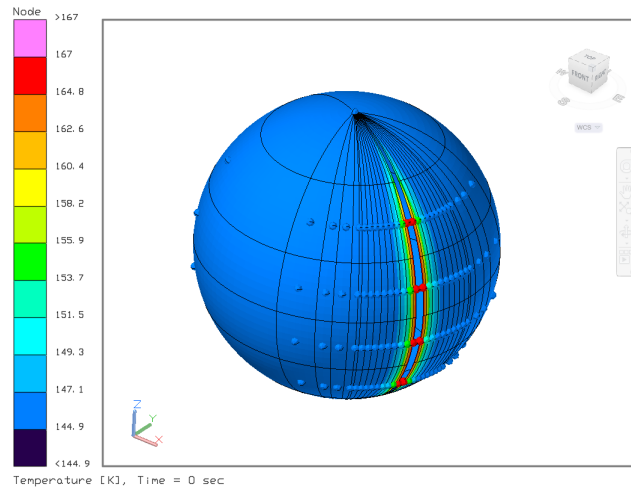


**Figure 76:** Case 7, layer 2.

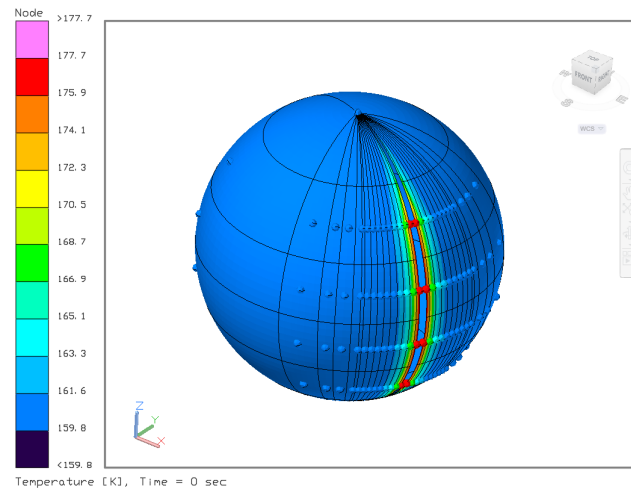


**Figure 77:** Case 7, layer 3.

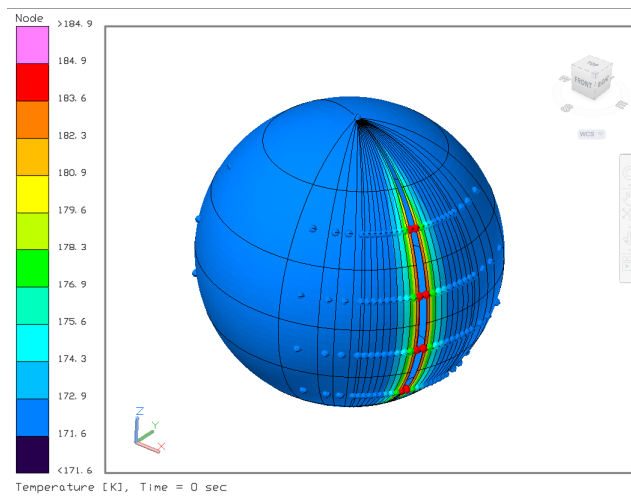


**Figure 78:** Case 7, layer 4.



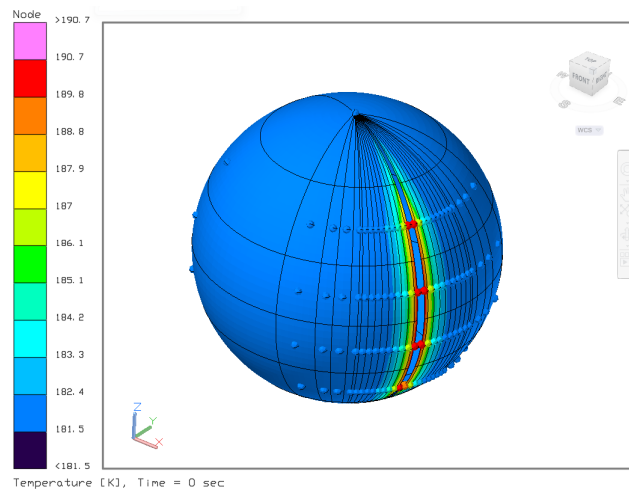


**Figure 79:** Case 7, layer 5.

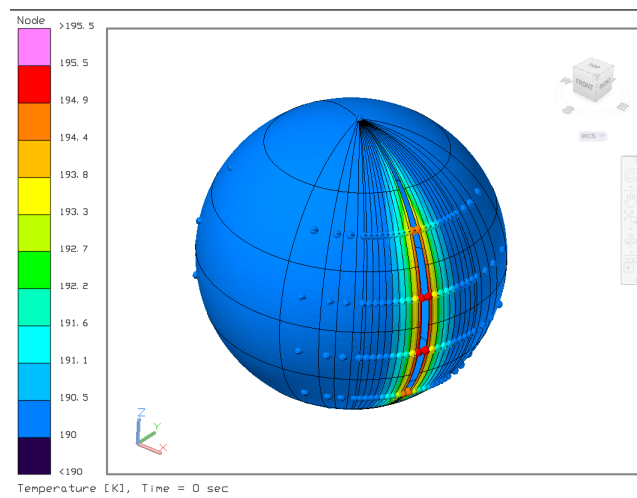


**Figure 80:** Case 7, layer 6.

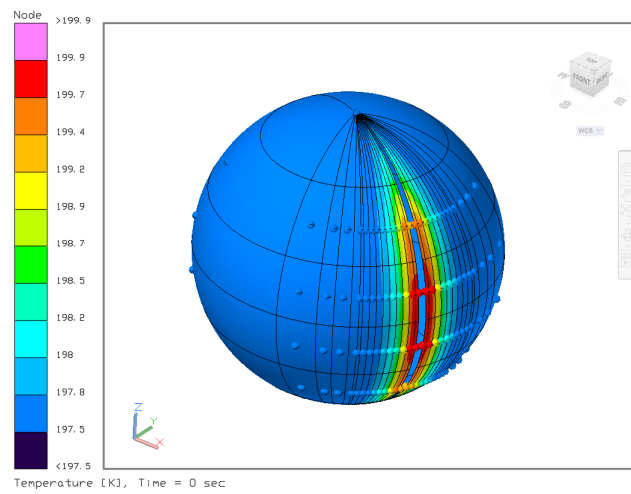


**Figure 81:** Case 7, layer 7.

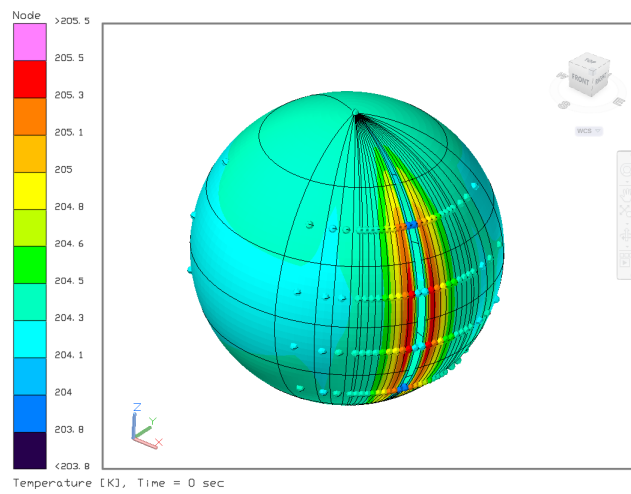


**Figure 82:** Case 7, layer 8.

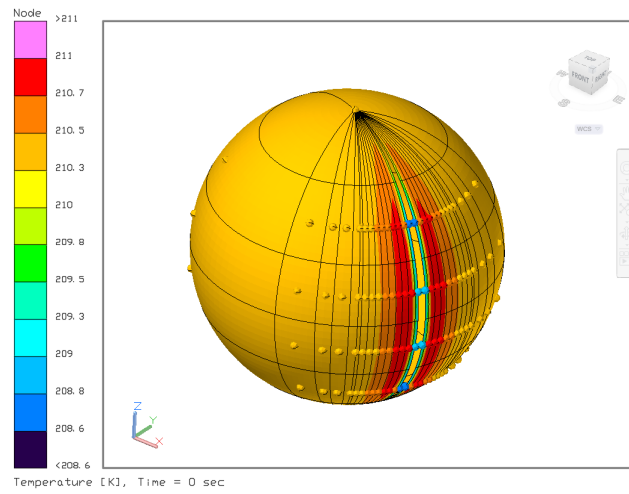


**Figure 83:** Case 7, layer 9.

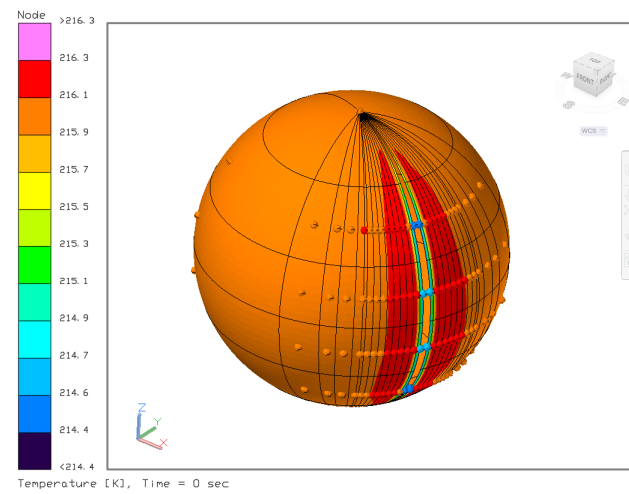


**Figure 84:** Case 7, layer 10.

Max	126.7199	L1.73
Min	108.9387	L1.20
Avg	110.7014	
Max	148.9588	L2.31
Min	125.9678	L2.98
Avg	128.4013	
Max	163.4431	L3.115
Min	141.1441	L3.15
Avg	143.656	
Max	173.6796	L4.115
Min	154.6641	L4.14
Avg	156.9424	
Max	181.6469	L5.21
Min	166.7718	L5.61
Avg	168.6566	
Max	188.3669	L6.105
Min	177.6419	L6.56
Avg	179.1062	
Max	194.3366	L7.106
Min	187.4999	L7.19
Avg	188.5355	
Max	200.0293	L8.64
Min	196.4837	L8.88
Avg	197.1306	
Max	206.3407	L9.62
Min	204.7467	L9.9
Avg	205.0608	
Max	213.1213	L10.97
Min	211.712	L10.83
Avg	212.466	

**Figure 85:** Temperature profile with maximum and minimum temperature node0.s being shown for case 7.

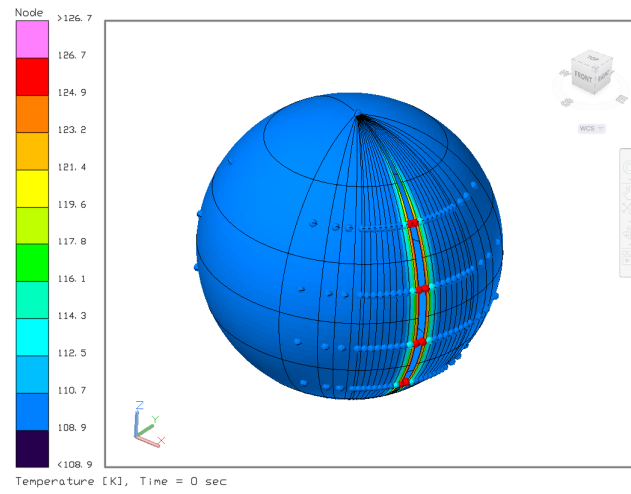


**Figure 86:** Case 8, layer 1.

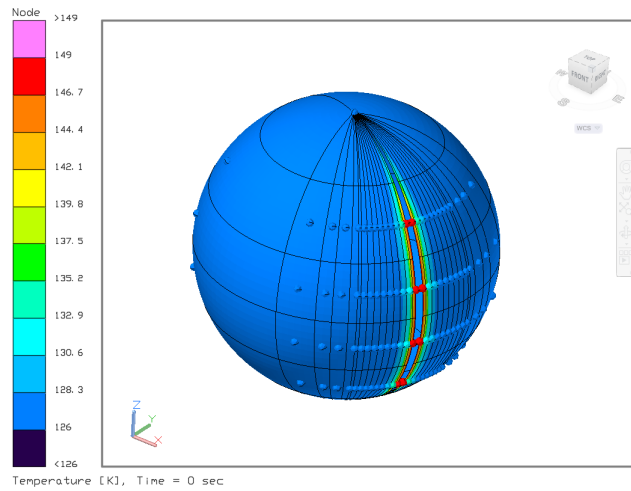


**Figure 87:** Case 8, layer 2.

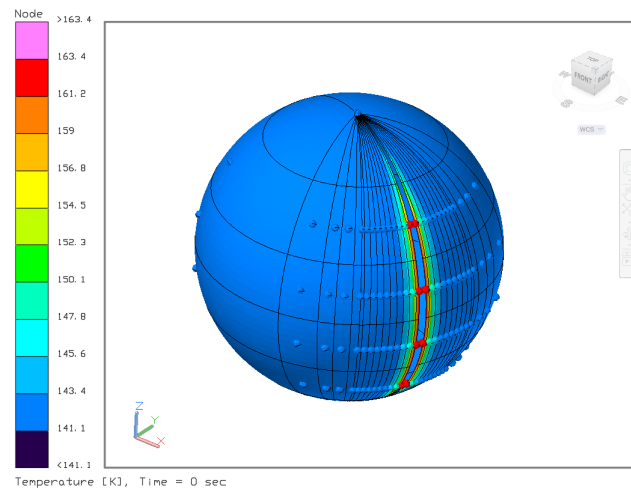


**Figure 88:** Case 8, layer 3.

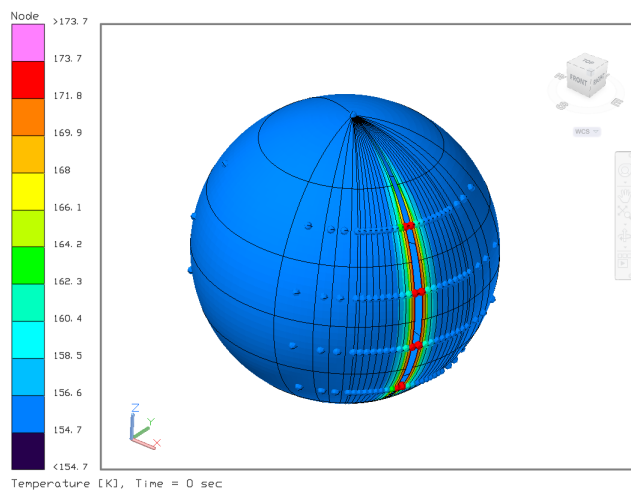


**Figure 89:** Case 8, layer 4.

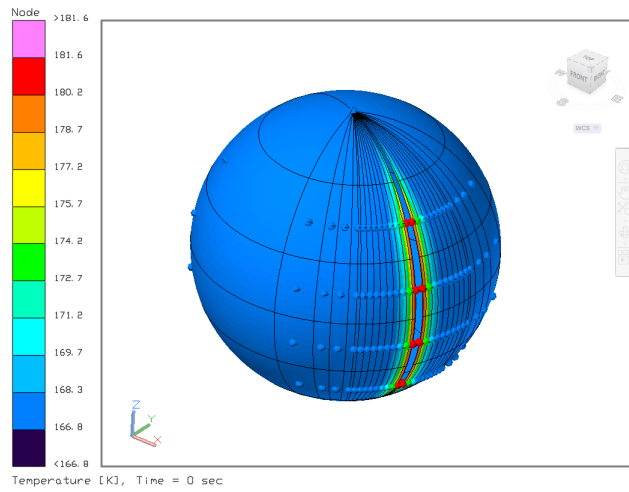


**Figure 90:** Case 8, layer 5.

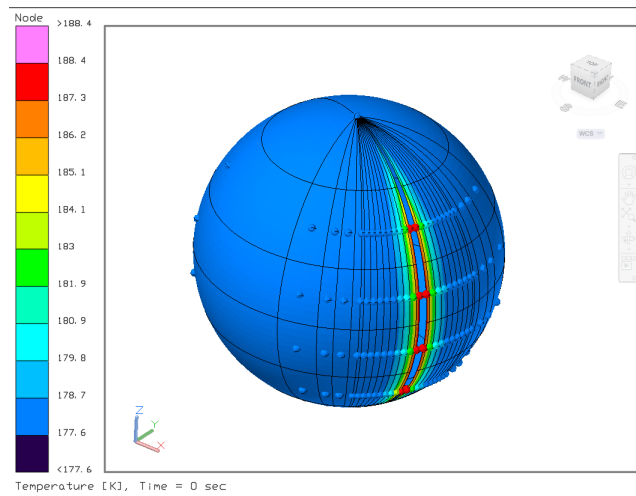


**Figure 91:** Case 8, layer 6.

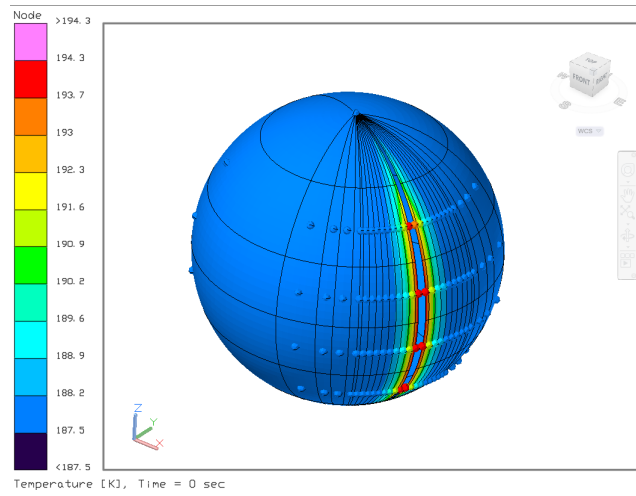


**Figure 92:** Case 8, layer 7.

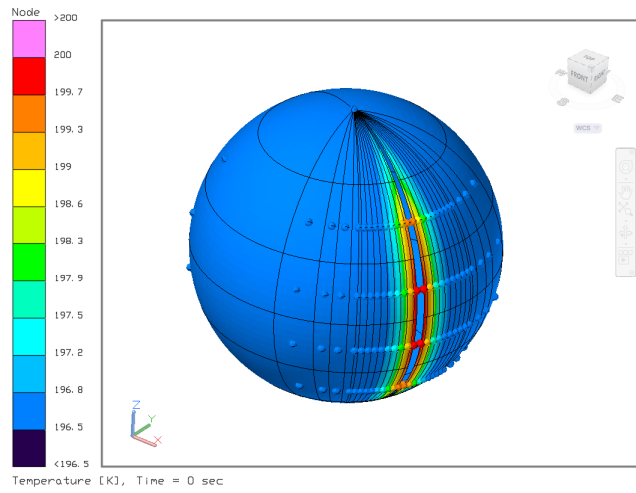


**Figure 93:** Case 8, layer 8.



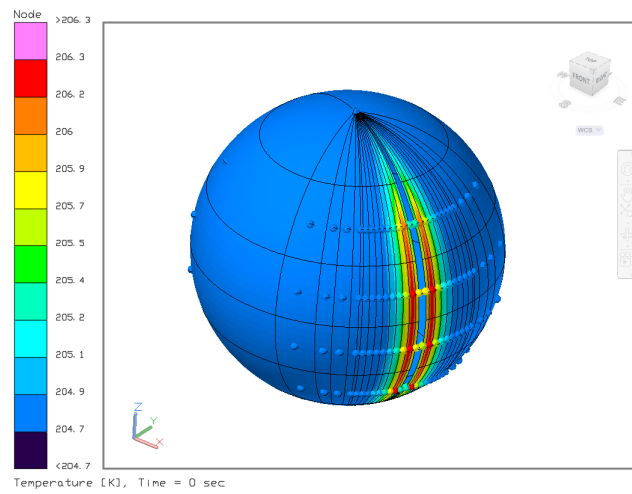


**Figure 94:** Case 8, layer 9.

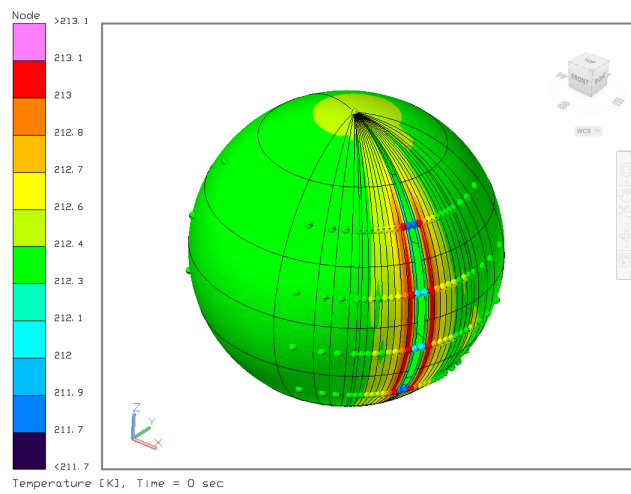


**Figure 95:** Case 8, layer 10.

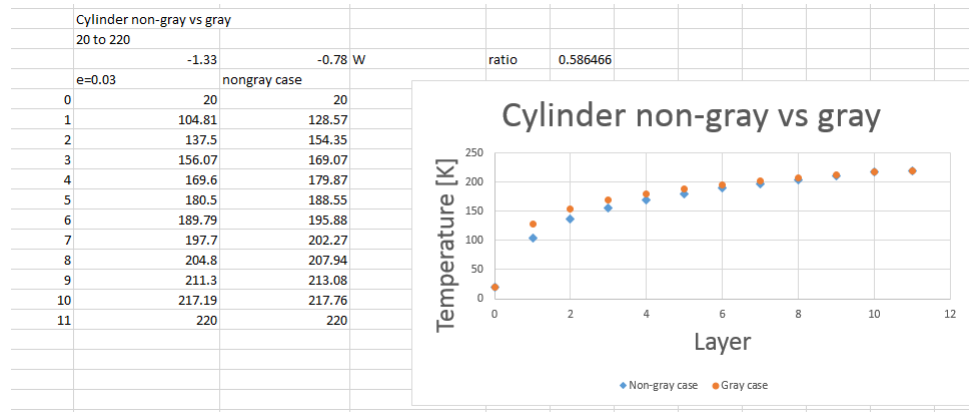


**Figure 96:** Cylinder gray vs non-gray

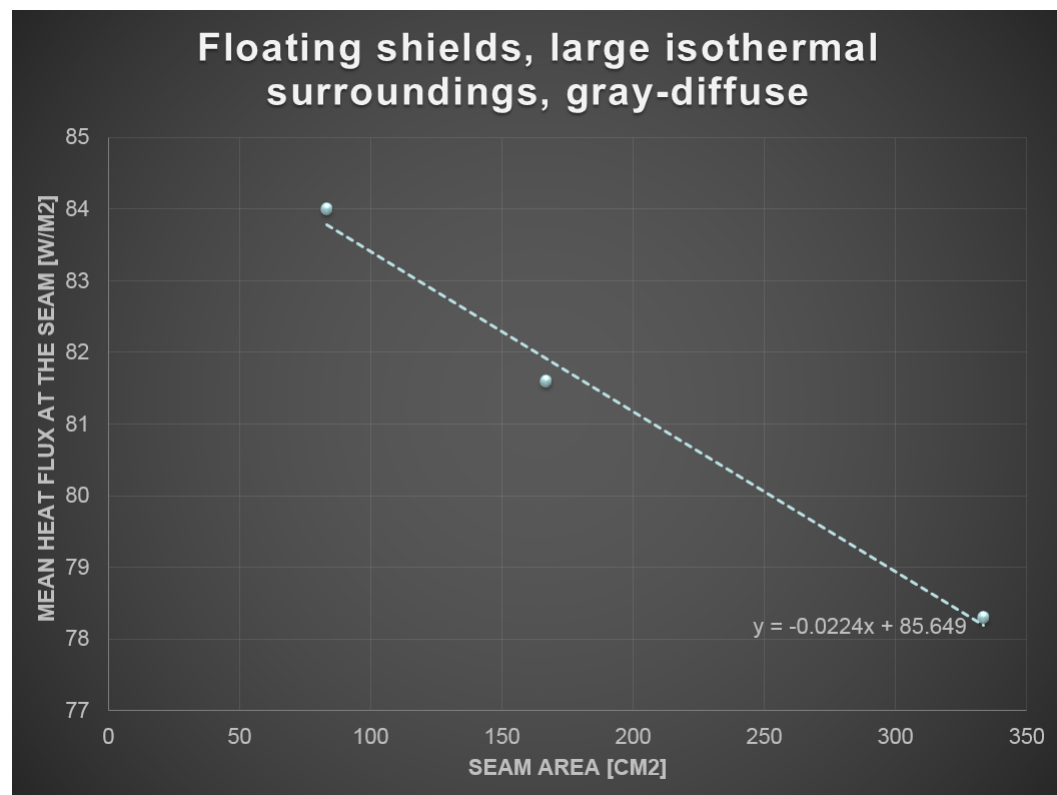


**Figure 97:** Cylinder gray vs non-gray